

AFRL-AFOSR-UK-TR-2013-0047



**Microscale Heat Transfer Enhancement using Spinodal
Decomposition of Binary Liquid Mixtures: A Collaborative
Modeling/Experimental Approach**

**Gian Paolo Beretta
Pietro Poesio**

**Universit`a degli Studi di Brescia,
Dipartimento di Ingegneria Meccanica e Industriale,
Via Branze 38,
Brescia, 25123 ITALY**

EOARD Grant 11-3068

Report Date: September 2013

Final Report from 1 September 2011 to 31 August 2013

Distribution Statement A: Approved for public release distribution is unlimited.

**Air Force Research Laboratory
Air Force Office of Scientific Research
European Office of Aerospace Research and Development
Unit 4515 Box 14, APO AE 09421**

REPORT DOCUMENTATION PAGE				Form Approved OMB No. 0704-0188	
<small>Public reporting burden for this collection of information is estimated to average 1 hour per response, including the time for reviewing instructions, searching existing data sources, gathering and maintaining the data needed, and completing and reviewing the collection of information. Send comments regarding this burden estimate or any other aspect of this collection of information, including suggestions for reducing the burden, to Department of Defense, Washington Headquarters Services, Directorate for Information Operations and Reports (0704-0188), 1215 Jefferson Davis Highway, Suite 1204, Arlington, VA 22202-4302. Respondents should be aware that notwithstanding any other provision of law, no person shall be subject to any penalty for failing to comply with a collection of information if it does not display a currently valid OMB control number.</small> PLEASE DO NOT RETURN YOUR FORM TO THE ABOVE ADDRESS.					
1. REPORT DATE (DD-MM-YYYY) 23 September 2013		2. REPORT TYPE Final Report		3. DATES COVERED (From – To) 1 September 2011 – 31 August 2013	
4. TITLE AND SUBTITLE Microscale Heat Transfer Enhancement using Spinodal Decomposition of Binary Liquid Mixtures: A Collaborative Modeling/Experimental Approach				5a. CONTRACT NUMBER FA8655-11-1-3068	
				5b. GRANT NUMBER Grant 11-3068	
				5c. PROGRAM ELEMENT NUMBER 61102F	
				5d. PROJECT NUMBER	
6. AUTHOR(S) Gian Paolo Beretta Pietro Poesio				5d. TASK NUMBER	
				5e. WORK UNIT NUMBER	
7. PERFORMING ORGANIZATION NAME(S) AND ADDRESS(ES) Universit`a degli Studi di Brescia, Dipartimento di Ingegneria Meccanica e Industriale, Via Branze 38, Brescia, 25123 ITALY				8. PERFORMING ORGANIZATION REPORT NUMBER N/A	
9. SPONSORING/MONITORING AGENCY NAME(S) AND ADDRESS(ES) EOARD Unit 4515 APO AE 09421-4515				10. SPONSOR/MONITOR'S ACRONYM(S) AFRL/AFOSR/IOE (EOARD)	
				11. SPONSOR/MONITOR'S REPORT NUMBER(S) AFRL-AFOSR-UK-TR-2013-0047	
12. DISTRIBUTION/AVAILABILITY STATEMENT Distribution A: Approved for public release; distribution is unlimited.					
13. SUPPLEMENTARY NOTES					
14. ABSTRACT <p>The aim of the project has been the analysis and development of a spinodal decomposition technology to enhance the heat transfer efficiency in microdevices. Poesio et al. (2007) had shown that the cooling (down to a given temperature) of a closed cell filled with a liquid-liquid mixture undergoing spinodal decomposition can be achieved ten-times faster compared to the case of a cell filled with a single-phase fluid. This effect can be explained as the result of (spinodal-decomposition induced) convective motion: the free energy released during spinodal decomposition acts as a driving force for the phase separation, leading to the spontaneous formation of single-phase domains which then proceed to grow and coalesce; this convective motion enhances the transport of internal energy and results in an appreciable heat transfer enhancement. Based on the proof-of-concept fundamental experiments in Poesio et al. (2006), Poesio et al. (2007), Poesio et al. (2009), and Faris`e et al. (2012), this technology was awaiting use in a configuration more relevant from the applications point of view, such as in a flowing system. The ultimate goal has been the design of a proof-of-concept micro/mini heat exchanger based on liquid-liquid spinodal decomposition. The project lasted for three years with the first year sponsored by the Asian Office of Aerospace Research and Development, AOARD (Grant FA2386-10-1-4146). Continued with the European office, EOARD (Grant FA8655-11-1-3068), and completed in 2013. The work has accomplished two main objectives: (1) demonstrated and analyzed heat transfer in small-scale heat exchangers; and (2) conducted numerical modeling as a precursor to a design tool. Since the currently available modeling tools require years of computational time to complete the simulation of a practical-sized device, this effort only started developing a novel theoretical modeling approach that eventually will lead to the design of efficient heat exchangers.</p>					
15. SUBJECT TERMS EOARD, thermodynamics, thermal management, spinodal decomposition, heat transfer efficiency, heat exchangers					
16. SECURITY CLASSIFICATION OF:			17. LIMITATION OF ABSTRACT SAR	18. NUMBER OF PAGES 58	19a. NAME OF RESPONSIBLE PERSON Kevin Bollino
a. REPORT UNCLAS	b. ABSTRACT UNCLAS	c. THIS PAGE UNCLAS			19b. TELEPHONE NUMBER (Include area code) +44 (0)1895 616163

Final report on project FA8655-11-1-3068

**Microscale heat transfer enhancement
using spinodal decomposition of binary
liquid mixtures: a collaborative
modeling/experimental approach**

Gian Paolo Beretta

Pietro Poesio

Università degli Studi di Brescia, Dipartimento di Ingegneria
Meccanica e Industriale, Via Branze 38, 25123, Brescia, Italy
September 23, 2013

Contents

List of Figures	3
1 Introduction	6
1.1 Theory	8
1.1.1 Spinodal decomposition	8
1.1.2 Pressure drop correlation	8
2 Methods, Assumptions, and Procedures	9
2.1 Experimental Approach	9
2.1.1 Heat Transfer Enhancement Measurements	9
2.1.2 Pressure Drop Measurement	17
2.1.3 Visualizations	23
2.2 Numerical Approach	24
2.2.1 Synthetic concentration and velocity fields to model trans- port enhancement effects due to Korteweg micro-agitation during spinodal decomposition	24
3 Results	26
3.1 Experimental Results	26
3.1.1 Heat Transfer Enhancement Measurements	26
3.2 Spinodal decomposition visualization	30
3.3 Pressure Drop Measurement	33
3.4 Visualizations	36
3.4.1 PTV-like post processing	36
3.4.2 PIV-like post processing	38
3.5 Numerical Results	41
4 Conclusions	46
4.1 Future Developments	51
4.2 Articles and Conference Proceedings Produced So Far and Ac- knowledging this Grant	53

List of Figures

1	Miscibility-gap phase diagram for Acetone-Hexadecane mixtures.	10
2	Sketch of the experimental set-up.	10
3	The three heat exchangers we tested in our experimental setup. .	12
4	T_{bath} versus time during the validation test to determine $\dot{Q}_{\text{el}}^{\text{Max}}$. .	14
5	Percentage difference $\Delta = (\dot{Q}_{\text{Joule}} - \dot{Q}_{\text{testsection}} - \dot{Q}_{\text{inletpipe}} - \dot{Q}_{\text{outletpipe}}) / \dot{Q}_{\text{Joule}}$.	15
6	Total exchange area in our micro channel heat exchanger.	15
7	Comparison between theoretical and experimental Nusselt numbers in a single-channel test with water, $T_{\text{bath}}=35^{\circ}\text{C}$ and $T_{\text{Cu}}=20^{\circ}\text{C}$.	16
8	Sketch of the experimental set-up.	18
9	Sketch of the glass channel test section.	18
10	Sketch of the stainless steel capillary test section.	19
11	Microchannel used to measure pressure drops.	19
12	Counter current pipe in pipe heat exchanger used with the stainless steel capillary.	20
13	Water Pressure Drop with $T_{\text{inlet}} 30^{\circ}\text{C}$ in the glass test section. .	21
14	Water Pressure Drop with $T_{\text{inlet}} 30^{\circ}\text{C}$ in the steel capillary. . . .	22
15	Sketch of the experimental set-up.	22
16	Microchannel used to measure pressure drops.	23
17	Structure factor of the concentration field obtained from the solution of the full CHNSE model equations normalized over the characteristic length scale of the growing domains.	25
18	Comparison between theoretical and experimental Nusselt numbers in a single-channel with pure acetone with $T_{\text{bath}}=35^{\circ}\text{C}$ and $T_{\text{Cu}}=20^{\circ}\text{C}$	27
19	Comparison between theoretical and experimental Nusselt numbers in a single-channel with pure hexadecane with $T_{\text{bath}}=35^{\circ}\text{C}$ and $T_{\text{Cu}}=20^{\circ}\text{C}$	28
20	Absorbed electrical power versus flow-rate with $T_{\text{bath}}=35^{\circ}\text{C}$ and $T_{\text{Cu}}=25^{\circ}\text{C}$, measured for single channel flow of pure acetone, pure hexadecane, and a mixture of acetone and hexadecane with critical mole fraction ($y_{\text{acn}} = 0.799$). Mixture data and pure-component data show no important difference since spinodal decomposition occurs mildish for $T_{\text{Cu}}=25^{\circ}\text{C}$	28
21	Comparison between theoretical and experimental Nusselt numbers in a single-channel with a critical mixture of acetone and hexadecane, $T_{\text{bath}}=35^{\circ}\text{C}$ and $T_{\text{Cu}}=20^{\circ}\text{C}$. Here the quench is deep enough that spinodal decomposition induces a heat transfer enhancement, except for the first five experimental point at low flow rates (that we report for completeness, but may be affected by large errors, see section 2.1.1.3.2).	29
22	Absorbed electrical power versus flow rate measured for single channel flow with $T_{\text{bath}}=35^{\circ}\text{C}$ and $T_{\text{Cu}}=20^{\circ}\text{C}$. Compared with Fig. 20 the data for the mixture show enhanced heat transfer as expected since vigorous spinodal decomposition does occur for $T_{\text{Cu}}=20^{\circ}\text{C}$	30
23	Electric power absorbed by the parallel heat exchanger with $T_{\text{bath}}=35^{\circ}\text{C}$ and $T_{\text{Cu}}=25^{\circ}\text{C}$, 2°C quench mild decomposition.	31

24	Electric power absorbed for the U-shape heat exchanger with $T_{\text{bath}}=35^{\circ}\text{C}$ and $T_{\text{Cu}}=25^{\circ}\text{C}$, 2°C quench mild decomposition. . .	31
25	Electric power absorbed by the parallel heat exchanger with $T_{\text{bath}}=35^{\circ}\text{C}$ and $T_{\text{Cu}}=20^{\circ}\text{C}$, 7°C quench vigorous decomposition.	31
26	Electric power absorbed for the U-shape heat exchanger with $T_{\text{bath}}=35^{\circ}\text{C}$ and $T_{\text{Cu}}=20^{\circ}\text{C}$, 7°C quench vigorous decomposition.	31
27	Heat-transfer Augmentation Factor (AF) as defined by 20, computed from the data in Figs. 23 to 26.	32
28	Effect of quench depth on the vigorousness of the spinodal decomposition of an acetone-hexadecane mixture in a single-channel flow.	32
29	Ideal and real behavior of acetone and hexadecane in the micro-channel	33
30	Mixture at room temperature	34
31	Ideal and real behavior of acetone and hexadecane in the micro-channel	35
32	Mixture at room temperature	36
33	Sequence of spinodal decomposition at 22°C	37
34	Sequence of spinodal decomposition at room temperature	39
35	Cleaning of the frames	40
36	Phase Growth	41
37	PTV frame 1	42
38	PTV frame 2	43
39	Sequence of isolated phases	44
40	Cleaning of the frames	45
41	Speed and growth of the phases	46
42	Image post-processed with the PIV algorithm	47
43	Turbulence spectrum (EXPERIMENTAL)	47
44	Turbulence spectrum (EXPERIMENTAL/NUMERICAL)	48
45	Comparison of the Margules parameter (where $\Psi = \frac{2T}{T_c}$) profile of the DNS calculation for $\text{Pe}=1000$ with the analytical profile with no convection ($\text{Pe}=0$) at one selected time step	48
46	Comparison between the Margules parameter profiles (where $\Psi = \frac{2T}{T_c}$) of the SCVF approach and $\text{Pe}=1000$ and of the analytical profile with no convection ($\text{Pe}=0$) at one selected time step . . .	49
47	Comparison between the Margules parameter (where $\Psi = \frac{2T}{T_c}$) profiles of the SCFV approach and $\text{Pe}=1000$ and of the analytical profile with no convection ($\text{Pe}=0$) at one selected time step . . .	49
48	Behavior of structure factor for the cross correlation of concentration and velocity	50
49	Behavior of structure factor for the cross correlation of temperature and velocity	50
50	Behavior of the Korteweg force structure factor for two different Peclet number and for different times	51
51	Heat-transfer Augmentation Factor vs Re.	52
52	Water and Triethylamine mixture Phase Diagram	52

Summary

The aim of the project has been the analysis and development of a spinodal decomposition technology to enhance the heat transfer efficiency in microdevices. Poesio et al. (2007) ([Poesio *et al.* (2007)]) had shown that the cooling (down to a given temperature) of a closed cell filled with a liquid-liquid mixture undergoing spinodal decomposition can be achieved ten times faster compared to the case of a cell filled with a single-phase fluid. This effect can be explained as the result of (spinodal-decomposition induced) convective motion: the free energy released during spinodal decomposition acts as a driving force for the phase separation, leading to the spontaneous formation of single-phase domains which then proceed to grow and coalesce; this convective motion enhances the transport of internal energy and results in an appreciable heat transfer enhancement. Based on our proof-of-concept fundamental experiments in [Poesio *et al.* (2006)], [Poesio *et al.* (2007)], [Poesio *et al.* (2009)], [Farisé *et al.* (2012)] this technology was awaiting use in a configuration more relevant from the applications point of view, such as in a flowing system. The ultimate goal has been the design of a proof-of-concept micro/mini heat exchanger based on liquid-liquid spinodal decomposition. The project was supposed for the last three years. AOARD (Grant FA2386-10-1-4146) sponsored the first year. The project has then been taken up by EOARD (Grant FA8655-11-1-3068) for the two remaining years and is now complete. The present document is the final report of the last two years of work. The work has followed two main lines:

- experimental investigation of heat transfer in small scale heat exchangers;
- numerical modeling to build a designing tool. Since the currently available modeling tools would require years of computational time to complete the simulation of a practical-size device, we started developing a novel theoretical modeling approach that eventually will allow us to design efficient heat exchangers.

In addition to Prof. G.P. Beretta and Prof. P. Poesio, the work has been done by:

- Dr. D. Molin, post-doc hired on the funds provided by AOARD and EOARD, who worked on the numerical simulations;
- S. Farisé, Ph.D. student hired on internal UniBS funds, who carried out most of the experimental work.
- M. Neri, Ph.D. student partially hired on EOARD funds, who helped carry out some of the latest experimental work.

Co-operation with Prof. N.G. Hadjiconstantinou (M.I.T.) has proven very useful in the numerical modeling of the problem.

1 Introduction

With the constant rush for miniaturization, especially in electronics, and the more widespread use of integrated systems, we need technologies that allow to exchange a large amount of heat in small devices and with the highest possible efficiency.

Tuckerman and Pease ([Tuckerman and Pease (1981)]) first introduced the concept of micro channel heat sink, and since then several technologies have been developed to exchange heat more effectively.

An important distinction must be made between technologies that use a single-phase flow and those that use multiphase flows. Among the latter another distinction is between multiphase flows of a single constituent and flows of non-miscible components. Tuckerman and Pease ([Tuckerman and Pease (1981)]) optimized the dimensions of the channels in terms of width and height for single-phase flow of water under the constraint of maximum allowable pressure drop and substrate surface temperature. They found that single-phase water-cooling could remove up to 790 W/cm^2 . A similar optimization process was done by ([Upadhye and Kandlikar (2004)]). The main problem with single-phase flow heat transfer in micro channels is the low Nusselt number obtained in laminar flow ([Shah and London (1978)]) – of the order of 4. Performance rises significantly using multi-phase technology. The study of boiling flows in a micro channel leads to much higher heat transfer coefficients due to the high heat of vaporization. Many authors ([Mudawar (2001)], [Mudawar and Bowers (1999)] and [Kandlikar (2005)]) showed that flow boiling can remove up to $10,000 \text{ W/cm}^2$.

While flow boiling is attractive because it delivers high heat flux at the constant temperature of the phase change, it can be difficult to control due to back flow, instabilities, and local dry-out ([Kandlikar (2002)]). Usually water is the working fluid, but the problem is that the saturation temperature is higher than the operating temperature of most electronics. The proposed solution is to use as working fluids refrigerants other than water, since their boiling temperature can be lower. Refrigerants, however, offer lower cooling capabilities due to lower specific heat and heat of vaporization.

Wang et al. ([Wang *et al.* (2004)]), to increase the Reynolds number, proposed the adoption of small nozzles that spray water on the surface to be cooled. Jet array helps to achieve uniform cooling of the chip surface and, on the other side, a carefully located single jet can provide highly localized cooling of hot spots on chips with nonuniform heat generation. Betz and Attinger ([Betz and Attinger (2010)]) investigated segmented flow as a way to enhance single-phase heat transfer with water in micro channels. Segmented flow is a periodic pattern of non-condensable bubbles and liquid slugs created by a T-junction with the injection of air in liquid-filled micro channels. Experiments and optimization studies have demonstrated that segmented flow could enhance heat transfer by up to 40% in a microchannel heat sink, in comparison with single-phase flow at the same liquid flow rate. The increase in performance is significant, but the system requires the simultaneous use of both water and compressed air. This complicates the design of the heat exchanger and the tuning of the flow rate to keep the system stable and optimized.

Experiments by Poesio et al. ([Poesio *et al.* (2007)]) have proved the concept that spinodal micro convection in a microfluidic setup can yield effective thermal diffusivities up to an order of magnitude higher than the molecular diffusivity

and that the enhancement effect is strongly dependent on how deep the mixture reaches into the unstable region of the phase diagram below the spinodal curve. Other experiments ([Gat *et al.* (2009)], [Di Fede *et al.* (2011)]) show that even in laminar flow in a 2 mm diameter pipe the effect can produce up to 40% enhancement.

Spinodal decomposition (SD) occurs when a partially-miscible fluid mixture, initially in a homogeneous region of the phase diagram, is rapidly driven by a temperature or composition change into the miscibility gap, well into the spinodal region where the local equilibrium states are unstable and have 'ready' free energy. Then, as soon as fluctuations in the local composition field trigger the instability, the mixture starts to separate (slowly) by diffusion driven by the dissipation of only part of the 'ready' free energy while the remainder gets converted into surface energy stored in the thin interfacial regions of the two-phase structure which begins to form. This typical structure is bicontinuous and dendritic-like if the initial composition is critical, drop-like if it is off-critical. Once formed, the single-phase patches are pushed around by capillary (Korteweg) body forces.

That Korteweg stresses induce a velocity field that has been proved experimentally ([Mauri *et al.* (1996)], [Poesio *et al.* (2006)], [Poesio *et al.* (2009)]) but not yet fully characterized. During SD, this motion pushes single-phase patches towards one another thus favoring coalescence, whereby part of the free energy stored in the interfacial regions gets rapidly converted into further kinetic energy. For high-viscosity mixtures, such as polymer melts or liquid metals, this kinetic energy is immediately dissipated and the balance between Korteweg and viscous forces make the domains grow in time as $R \approx t^{1/3}$, where R is the average domain size ([Siggia (1979)]). For low-viscosity mixtures, instead, this intermediate stage of SD is convection-driven and the balance between Korteweg and convective forces make the domains grow with time as $R \approx t^1$. Eventually, domains become large enough that buoyancy becomes more important and dominates the remaining coalescence until complete separation.

Several techniques have been used to model liquid-liquid SD, including Molecular Dynamics, Monte Carlo and Lattice Boltzmann simulations. But the most successful has been the Phase-Field model approach ([Ginzburg and Landau (1979)]) and its variants known as the van der Waals Square-Gradient Model ([Rowlinson and Waals (1893)], [Korteweg (1893)]), the Cahn-Hilliard model ([Cahn and Hilliard (1958)]), the H Model ([Kawasaki (1958)], [Hohenberg and Halperin (1977)]) the Diffuse-Interface model ([Antanovskii (1996)]). In such phase-field models there are no sharp interfaces. The interface between domains of different composition is described by the continuous variation of an order parameter (here the mole fraction ϕ) so that fluid properties vary smoothly across the interface. Surface tension effects are incorporated in the well-known set of Cahn-Hilliard-Navier-Stokes (CHNS) equations through a (Korteweg) body force that depends on the local gradient in composition. The approach has been successful to understand a variety of phenomena on a microscopic scale (phase-separation/mixing of binary/ternary fluids, boiling and condensation, domain growth in solidification of alloys, droplet coalescence and break-up, Rayleigh-Taylor instability, liquid-liquid jets and drops, polymer blends, contact angles/wetting, electrowetting, reactive flows, etc), notable reviews are found in ([D. M. Anderson *et al.* (1998)], [Emmerich (2008)]).

As shown by numerical simulations ([Molin and Mauri (2007)]), the CHNS

(Cahn-Hilliard/Navier-Stokes equation system) plus energy equations (CHNSE) do capture and confirm the heat transport enhancement effect induced by SD. But the applicability of the model equations to real micro heat exchanger devices is severely constrained by the need to resolve the smooth change in composition across the very thin interfaces between domains. Thus, the numerical simulation is feasible only on a very fine mesh, with a density of at least 3 to 5 grid points over the typical interface thickness of the order of 2 to 20 nanometers, so that even to model a smallest microfluidic device of 10 x 10 x 50 micron would require 10^{12} grid points. In other words, the multi-scale nature of SD arises from the large separation between the smallest length scale (interface thickness) and scale of the device. Moreover, the full CHNSE model contains strong non-linearities that make the numerical problem unstable and requires also very fine time steps. It is for these reasons that although homogeneous SD has been rather extensively investigated, studies of SD in three-dimensional devices of realistic size have not been possible.

1.1 Theory

1.1.1 Spinodal decomposition

Spinodal decomposition is the spontaneous process whereby an unstable partially miscible liquid mixture relaxes toward a lower free energy (stable) equilibrium state. During this process, an initially homogeneous liquid solution of a given composition spontaneously changes from an unstable single-phase to a two-phase stable state consisting of two separated liquid phases, of different compositions, in mutual equilibrium. This is possible only if the overall Gibbs free energy of the two separated phases is lower than that of the initial single-phase mixture. When an initially homogeneous liquid mixture at high temperature is cooled rapidly across the coexistence (binodal) curve into the two-phase region, it undergoes phase segregation (demixing) either by nucleation or by spinodal decomposition. Nucleation occurs when quenching takes the system in a metastable equilibrium state (between the binodal and the spinodal curve): it is an activated process and a free energy barrier must be overcome in order to form critical nuclei that later grow and coalesce. Spinodal decomposition, instead, occurs spontaneously, without an energy barrier to overcome (the initial state is below the spinodal curve): all the concentration fluctuations are amplified regardless of their size and wavelength. If the mechanism of segregation is convection dominated, as occurs for low viscosity systems, drops move against each others under the influence of non-equilibrium capillary forces, the so-called Korteweg stresses [Poesio *et al.* (2009)]. Recently, it has been shown that this self-induced disordered bulk flow can be used to increase the heat transfer rate both in a closed configuration [Poesio *et al.* (2007)] and in small pipe flow [Gat *et al.* (2009)] and [Di Fede *et al.* (2011)]. Also numerical simulations predict a significant increase in heat transfer [Molin and Mauri (2007)].

1.1.2 Pressure drop correlation

Usually the calculation of the theoretical pressure drop in a micro-channel is difficult because there are several disturbing effects due to the size of the channel. For this reason there are many articles that present equations to predict

the behavior of a fluid within a micro-channel. One of the most interesting studies is presented in [Bahramiet *al.* (2006)]: using the analytical solution for an elliptical duct and the concept of the de-Saint-Venant principle in torsion, they developed a general model for the prediction of pressure drop in micro-channels of arbitrary cross sectional shape. The main equation of this model relates pressure drop with the Reynolds number:

$$\Delta p = 16\pi^2 \mu Q I_p^* \frac{L}{A^2} \quad (1)$$

where $I_p^* = I_p/A$ is the specific polar momentum of inertia of the micro-channel cross section, Q is the volumetric flow rate, L and A the length and the cross sectional area of the micro-channel. Equivalently,

$$f Re_{\sqrt{A}} = 32\pi^2 I_p^* \frac{\sqrt{A}}{P} \quad (2)$$

where P is the perimeter of micro-channel section, f the friction factor and $Re_{\sqrt{A}}$ the Reynolds number based on the characteristic channel width \sqrt{A} .

The results indicate that the pressure drops is a function only of the geometry, the flow rate, the viscosity of the fluid, and the Reynolds number. The calculation shows a linear correlation between flow rate and pressure drop, too.

The validation of these results was made subsequently in [Bahramiet *al.* (2007)] and in [Akbari and Sinton (2009)], in which the experiments were carried out on micro-channels of various sections that have given results in agreement with those presented in [Bahramiet *al.* (2006)].

2 Methods, Assumptions, and Procedures

2.1 Experimental Approach

2.1.1 Heat Transfer Enhancement Measurements

2.1.1.1 Experimental setup We have used an 'UCST' (upper critical solution temperature) bi-component system made by a mixture of acetone and hexadecane (i.e. there is a critical temperature above which the components of the mixture are miscible in all proportions). This mixture has been selected because it is isopycnic, i.e., the two phases have almost the same density and, therefore, buoyancy effects are negligible. The components are also relatively non-toxic and can be safely used in relatively large volumes. The excess volume of this mixture has been considered negligible (it is lower than 5%). The minimal complete miscibility temperature as shown in Fig.1 is $27^\circ C$ and it is obtained using equal volume parts of the two components ($y_{acn} = 0.799$ in mole fraction of acetone).

Experimental data on the binodal curve are from [Machado and Rasmussen (1987)]. The spinodal curve is estimated using a two-parameter Margules-type model ([Di Fede *et al.* (2011)]). To measure the heat transfer enhancement effect due to spinodal decomposition, we have developed a closed-loop experimental set-up that allows us to pump the mixture from a hot thermostatic reservoir to the experimental test section where it is quenched by the thick pipe walls.

The test section consists of a micro heat exchanger. A Peltier cell is used to set and maintain the temperature of the cold side of the exchanger throughout

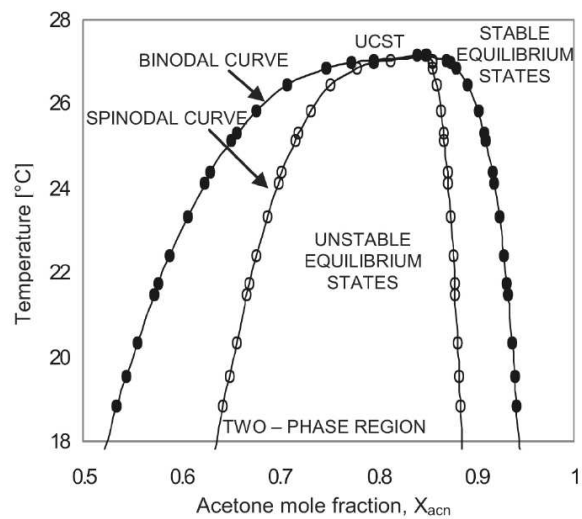


Figure 1: Miscibility-gap phase diagram for Acetone-Hexadecane mixtures.

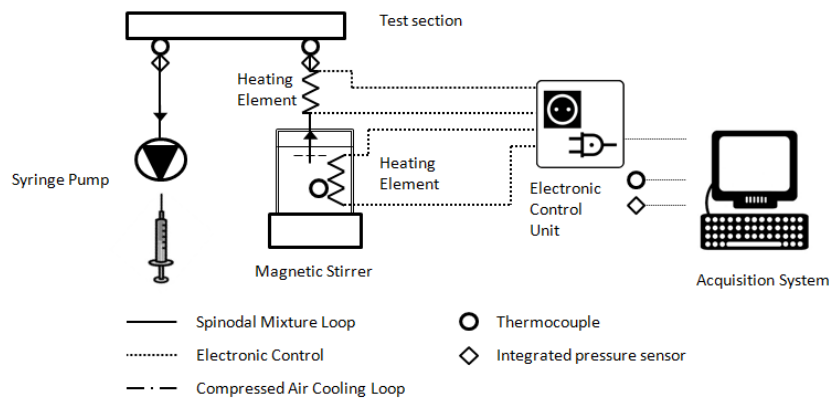


Figure 2: Sketch of the experimental set-up.

the test. The temperature of the cold side of the Peltier cell is kept constant by a computer controlled PID (Proportional Integral Derivative controller)(which regulates the duty cycle of the electric power supplied to the cell to keep the temperature constant). A thermostatic bath is used to cool the hot side of the cell. With these devices the temperature on the cold side of the Peltier cell can be kept in a range of $\pm 0.08^{\circ}\text{C}$ around the temperature setting. The system is controlled by a PC. Since we used this technique (that requires electric power and some sort of cooling) and not a second fluid to cool the mixture, we have no information about the actual amount of heat exchanged. We also need a controlled temperature at the inlet of the heat exchanger that must be above 27°C . So we built and used a second heating thermostat, also controlled by the PC and agitated with a magnetic stirrer, to keep the temperature as uniform as possible and to facilitate the mixing of the mixture. The inlet temperature imposed to the fluid was measured in an interval of $\pm 0.05^{\circ}\text{C}$ around the value set by the PC.

By reading the value of the duty cycle set by the PID feedback control we can estimate how much heat the hot thermostatic bath gives to the mixture reservoir to keep the temperature constant for the imposed conditions of cooling temperature and flow rate. We can, therefore, determine how much heat has been subtracted from the hot flow in the test section. Details of the simple calculation and validation of the technique are given in 2.1.1.3.1 and 2.1.1.3.2. With this procedure we introduce a smaller uncertainty than measuring the heat given to an hypothetical cold flow because we do not need to know the properties of the fluid, the flow rate and the position of the thermocouples. Our measurement uncertainties are only due to the voltage applied to the resistor and to the value of its resistance, and we are able to measure these quantities with an accuracy far greater than temperature and flow rate.

Our experiment has been done on 3 different types of heat exchangers.

The first and most simple is the single channel (Fig.3A): we cut a channel (section of $0.7 \times 0.7\text{mm}$ and 38mm long) in a piece of copper. The top and the bottom of the channel are sealed with a thin glass to record with a high-speed camera the test section. We placed a Peltier cell on each side of the channel to finely control the temperature and to be sure to have no gradient at all. A gradient would perturb the flow of the mixture and complicate the mechanics of heat transfer.

We used this heat exchanger for visualization and validation purposes: the exchange area is small so the difference in heat exchange is small, too. Therefore, the experimental uncertainty is greater than that obtained using the other heat exchangers.

Despite the single channel is very useful to understand the mechanism of spinodal decomposition via flow visualisation, its industrial applications are limited. We have built a second heat exchanger with 9 parallel channels ($0.7 \times 1.5\text{mm}$ tall and 72mm long). As the previous one this also has a glass top to view the flow pattern of the mixture during cooling. This set-up requires just a single Peltier cell placed behind the array of channels as shown in (Fig.3B).

The third heat exchanger (Fig.3C) is something very similar to the real heat sinks used to cool CPU's on PC's motherboards. It is a compact multi-channel array (14 channel) with a U shape. This too is sealed with a glass and cooled with a Peltier cell behind the channels.

We used a total of 5 (6 in the single channel configuration) thermocouples:

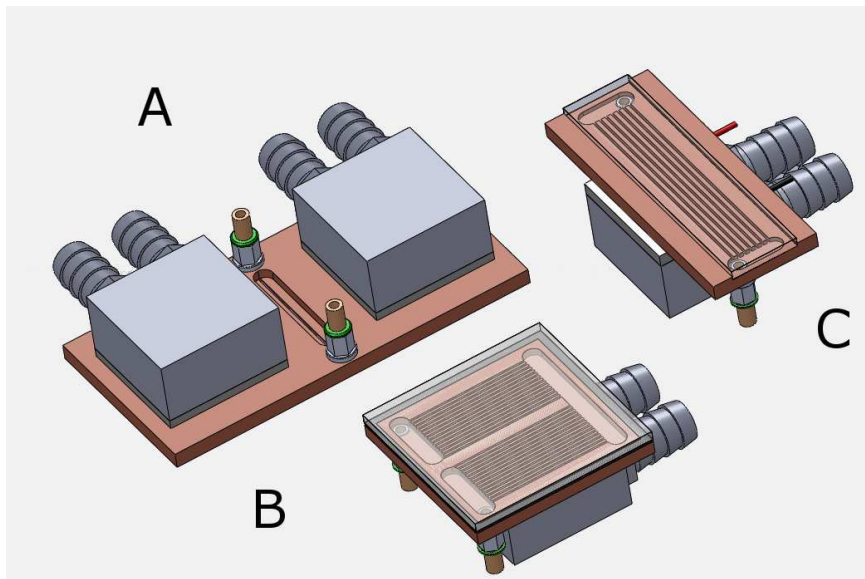


Figure 3: The three heat exchangers we tested in our experimental setup.

the first is placed in the mixture reservoir to constantly monitor the temperature of the hot mixture and as a feedback for the PID controller of the hot thermostatic bath; the second and the third are placed at the inlet and at the outlet of the heat exchanger; the forth is placed at the end of the outflow hose just before the hot reservoir to verify the heat balance; the last one (or the last two in the single channel set-up) is placed on the cold side of the Peltier cell to set and monitor the cold side temperature and as a feedback for the Peltier cell PID controller.

All thermocouples are type T, fabricated in our lab by wires coming from the same hank; each thermocouple is calibrated using a cold bath (0°C , ice/water), we could verify the resulting uncertainty to be in the range of $\pm 0.2^{\circ}\text{C}$. In addition, each measure presented in this paper has been obtained using the thermocouples differentially so that the uncertainty of measurement is reduced to $\pm 0.08^{\circ}\text{C}$.

In the following text we will only indicate the temperatures of the heated thermostatic reservoir and the cold side of the heat exchanger. Since the loop outside of the exchanger is very short and well insulated and the exchange area of the heat exchanger is relatively large, the temperatures of the inlet and the outlet of the test section (at least when the flow rate is greater than $10\text{ }\mu\text{l}/\text{min}$ as we explain in 2.1.1.3.2) coincide with the temperatures of the heated reservoir and the cold side of the heat exchanger.

2.1.1.2 Experimental procedure For each heat exchanger, tests were carried out with bi-distilled water (for validation purpose), pure acetone, pure hexadecane, and the spinodal mixture. The procedure is as follows:

- we switch on the thermostatic bath to cool the Peltier cell;

- we use the maximum flow rate available (30 ml/min) to ensure the best filling of the channels array;
- the flow rate is reduced to 10% of the maximum (3 ml/min);
- the temperature of the Peltier cell is brought to the desired value for the run;
- keeping fixed the temperature of the Peltier cell the heated reservoir temperature is increased to the desired value;
- we wait 5 minutes to reach a stable temperature condition and then we start the data acquisition;
- data for each flow rate are acquired for 5 minutes, then the flow rate is increased by 5%;
- the previous step is repeated until the maximum flow rate achievable in the test facility is reached;
- the temperature of the cold side of the heat exchanger is reduced and all the steps are repeated for the new temperature;
- the system is cleaned with solvent and dried with an air flow until complete drying.

The previous steps are repeated for each of the 4 fluids used in each heat exchanger.

2.1.1.3 Set-up validation

2.1.1.3.1 Heated reservoir maximum power The first parameter that we need to know during the validation of our system is the maximum electric power converted via Joule effect into heat power by the resistance of the heated reservoir. We need to know this exact value because we do not record step by step the electrical power value but only the duty cycle value, $DC(t)$, from which we estimate the converted power:

$$\dot{Q}_{el}(t) = DC(t)\dot{Q}_{el}^{Max}. \quad (3)$$

To evaluate this value we recorded a test section with the peristaltic pump off. By doing so and assuming that all the electrical power is converted into the heated bath, we can compute its value with this formula:

$$\dot{Q}_{el}^{Max} = mc_p \frac{dT}{dt}. \quad (4)$$

Fig. 4 shows the trend of the temperature of the hot thermostatic bath during the test. It increases, as expected, almost linearly with time because the properties of water in this temperature range are, to a good approximation, constant. We used 200ml of bi-distilled water and the frequency of the acquisition was 3Hz.

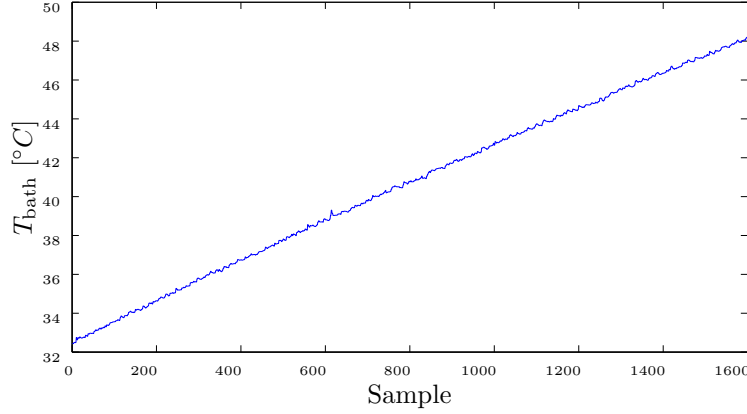


Figure 4: T_{bath} versus time during the validation test to determine $\dot{Q}_{\text{el}}^{\text{Max}}$.

2.1.1.3.2 Power balance validation As already explained, to measure the heat transfer in the test section we measure the electrical power sent to the resistor in the magnetically stirred thermostat.

This technique avoids the need to have precise estimates of the temperature-dependent thermo-physical properties of the mixture and which we know from [Di Fede *et al.* (2011)] are not known with good precision as a function of the temperature.

Our technique relies on the fact that all the electrical power converted to heat by the resistor in the hot thermostat is exchanged across the test section. To demonstrate this fact, we write the power balance for our closed system as follows

$$\dot{Q}_{\text{inletpipe}}^{\rightarrow} + \dot{Q}_{\text{testsection}}^{\rightarrow} + \dot{Q}_{\text{outletpipe}}^{\rightarrow} = \dot{Q}_{\text{Joule}}^{\leftarrow}, \quad (5)$$

$\dot{Q}_{\text{inletpipe}}^{\rightarrow}$ is the heat lost by the inlet pipe between the hot thermostat and the test section;

$\dot{Q}_{\text{testsection}}^{\rightarrow}$ is the heat exchanged in the test section;

$\dot{Q}_{\text{outletpipe}}^{\rightarrow}$ is the heat exchanged in the outlet pipe, between the test section and the hot thermostat;

$\dot{Q}_{\text{Joule}}^{\leftarrow}$ is the electrical power converted to heat by the resistor in the hot thermostat.

Fig. 5 shows the various contributions for the U-shaped multi-channel heat exchanger with water, $T_{\text{bath}}=35^{\circ}\text{C}$ and $T_{\text{Cu}}=25^{\circ}\text{C}$.

It shows that the difference between the supplied electrical power and the heat exchanged in the test section and in the inlet and outlet pipes is always within a 5%. It is possible to see that the error is greater for the lower fluid velocities for two main reasons: (1) the heat exchanged is smaller so the percentage error is greater; (2) it is caused by the imperfect insulation of the hot reservoir. The contribution of $\dot{Q}_{\text{inletpipe}}$ and $\dot{Q}_{\text{outletpipe}}$ is always less than 1W and almost constant during all tests. For this reason, we prefer to trust the data above 10 ml/min, but we will report all available data for the sake of completeness. After validating our system using water (it is the most stable fluid in the temperature range involved) we checked our assumption with the other pure fluids.

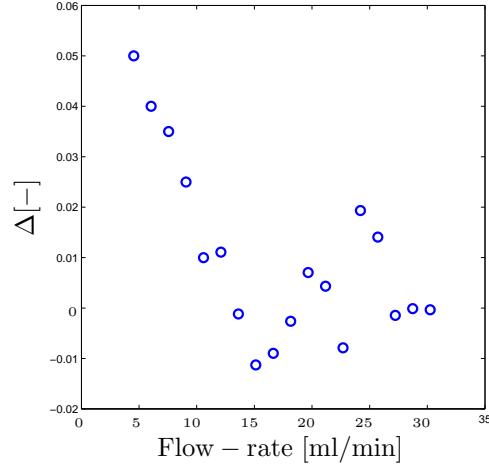


Figure 5: Percentage difference $\Delta = (\dot{Q}_{\text{Joule}} - \dot{Q}_{\text{testsection}} - \dot{Q}_{\text{inletpipe}} - \dot{Q}_{\text{outletpipe}})/\dot{Q}_{\text{Joule}}$.

We use the measured temperatures of the mixture at inlet and outlet of the test section only to calculate the Nusselt number according to Eq.6 below. For all subsequent correlations we use the value of \dot{Q}_{Joule} derived from the feedback control of the heated reservoir.

2.1.1.3.3 Single channel heat exchanger validation The single-channel exchanger is useful for our analysis because the theory behind the heat transfer in a square channel is well known, so comparing our results with the theoretical ones, we obtain a good feedback about the accuracy of our work.

The main problem we had in the data evaluation is the correct estimation of the inner exchange area of the channel. Due to geometry and sealing problems we could not put the thermocouples at the actual input and output of the channel, but we put them just outside the heat exchanger. This implies that the measured temperatures are not referred to the channel ends, but to the exchanger ones. Thus, the exchange area is greater than the channel area. Being difficult to measure directly, we measured the actual exchange area via software by using a 3D model.

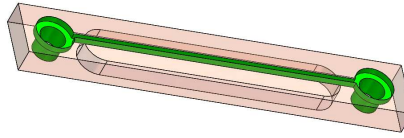


Figure 6: Total exchange area in our micro channel heat exchanger.

The experimental data are consistent with the area measured this way, therefore, we used it for all subsequent calculations.

Fig. 7 shows the results for the Nusselt number, the points refer to the experimental data, while the line refers to the theoretical correlation.

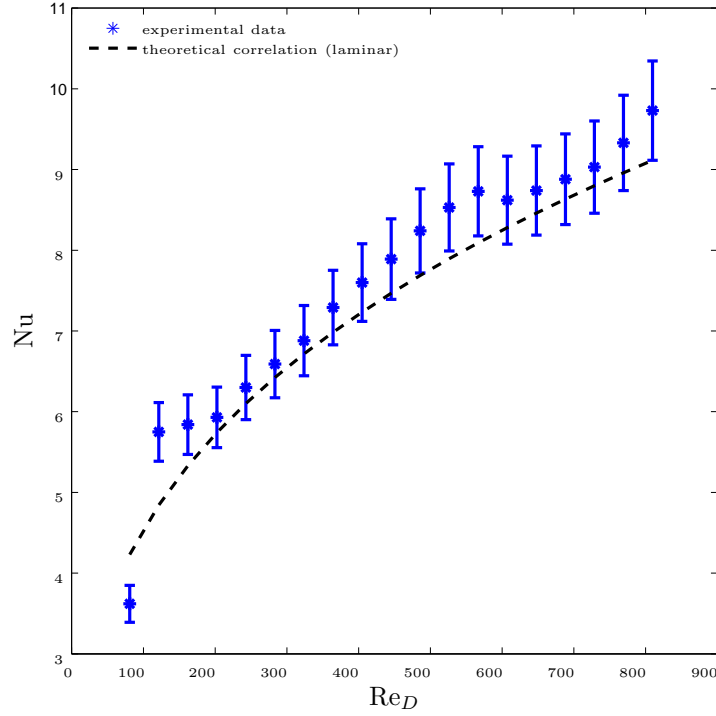


Figure 7: Comparison between theoretical and experimental Nusselt numbers in a single-channel test with water, $T_{\text{bath}}=35^{\circ}\text{C}$ and $T_{\text{Cu}}=20^{\circ}\text{C}$.

The Nusselt number is defined as:

$$Nu = \frac{\dot{m}c_p\Delta T_{\text{measured}}}{A\Delta T_{\text{lm}}} \frac{L}{k} \quad (6)$$

where $\Delta T_{\text{measured}}$ is the measured difference in temperature between inlet and outlet of the test section, ΔT_{lm} is the log-mean temperature difference between the mixture and the heat exchanger wall at inlet and outlet, \dot{m} is the measured mass flow rate, L is the hydraulic diameter of the test section, k the thermal conductivity of the mixture, c_p the specific heat, A the test-section heat-exchange area.

2.1.2 Pressure Drop Measurement

2.1.2.1 Experimental setup We used two different set-up configurations to measure the pressure drop of the mixture in different conditions.

In Fig. 8 is shown the set-up (common to the two different configurations) for heating the mixture uniformly and to make it reach the test section at a temperature higher than that of mixing is shown, so that the spinodal decomposition occurs in the micro channel. For the uniform heating of the mixture we used a magnetic stirrer, in combination with a resistance and a type T thermocouple. This allows us to keep the temperature of the mixture constant by a PID (Proportional Integral Derivative controller) control (Proportional Integral Derivative controller). The PID is a negative feedback system that takes an input signal from the system and compares it with the one set on the PC: in this way, it calculates the error and using a proportional component (considering current error), an integral (considering previous errors) and a derivative (considering the speed at which it changes) tries to drive it toward zero.

To avoid that the mixture gets in the channel at too low a temperature we have wrapped an electrical resistance around the connecting tube, with duty cycle of electrical power that has been controlled first manually, then using a PID control.

Next to the inlet and outlet thermocouples, we placed the inputs of the differential pressure sensor MPXV7002DP. This sensor has a range from -2 to 2 kPa and is connected to a PC to filter and capture the signal. The connection between the main tube and the sensor is made through two tubes filled with water with a needle at the end.

The mixture is pumped from the bath into the channel with a fixed flow rate by a syringe pump KDS Legato series 200, on which we use a 10 ml glass syringe. This pump has an accuracy of 0.35%.

The instruments are controlled by a LabVIEW interface, which produces the graphs of temperatures, pressure drop in the channel, and the PID signal for the heating bath.

We used two types of micro-channels, one is made by glass slides to allow the use of the microscope (Fig.11 left) and the other is a countercurrent flow heat exchanger (Fig.12 right).

The first is made up by two microscope slides glued together using anodic bonding. The first slide has two circular openings in which we pasted the input and output plugs, the second slide has a central groove made through a process of mechanical etching through which the mixture flows. This allows us to have very small passage sections that is helpful for measuring the pressure drop.

While using this glass test section the cooling of the mixture in the channel took place by a flow of compressed air cooled using a plate fin heat exchanger and a water cycle, keep at low temperature by a thermostatic bath (see Fig.9).

The latter is a stainless steel capillary (250 μm internal diameter, 500 μm outer diameter and 130 mm long) placed in the middle of a 8mm aluminum pipe. The cooling branch (the space between the aluminum pipe and the capillary) is fed by a peristaltic pump with water and to keep the inlet temperature constant a water-water heat exchanger (cooled by a thermostatic bath) is placed before the inlet (see Fig.10).

At both ends of the channel, we put two T-type thermocouples to acquire the temperature of inlet and outlet. Another T-type thermocouple was placed

in contact with the surface of the channel when we used the glass test sections and at the inlet of the cooling branch when we used the stainless steel capillary. Finally there is the thermocouple placed in the mixture reservoir to constantly monitor the temperature of the hot mixture and as a feedback for the PID controller of the hot thermostatic bath.

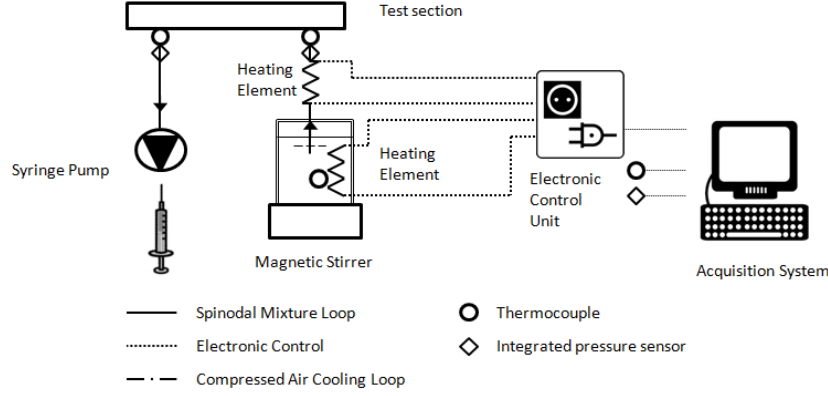


Figure 8: Sketch of the experimental set-up.

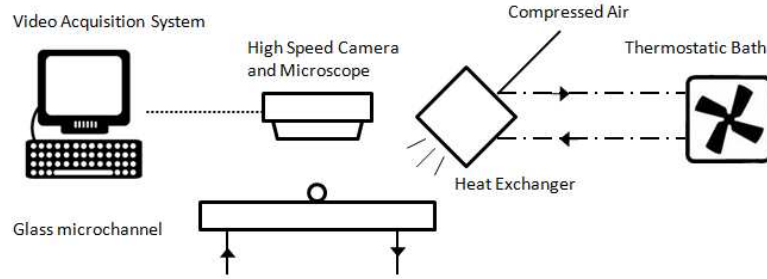


Figure 9: Sketch of the glass channel test section.

All thermocouples are type T, fabricated in our lab by wires coming from the same hank; each thermocouple is calibrated using a cold bath (0°C , ice/water), we could verify the resulting uncertainty to be in the range of $\pm 0.2^{\circ}\text{C}$. In addition, each measure presented in this paper has been obtained using the thermocouples differentially so that the uncertainty of measurement is reduced to $\pm 0.08^{\circ}\text{C}$.

2.1.2.2 Experimental procedure We repeat this test for pure water, pure acetone, pure hexadecane, and the acetone-hexadecane mixture at different cooling conditions.

The procedure is as follows:

- the temperature of the liquid is set at 32°C in the heating bath;

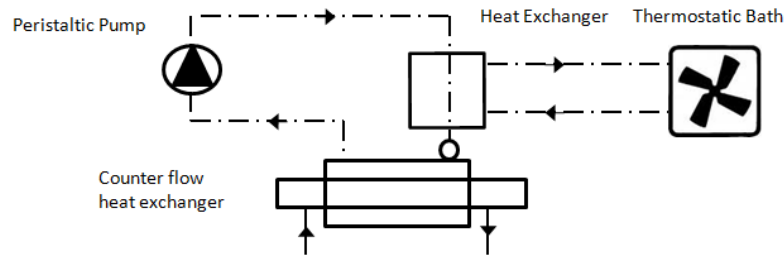


Figure 10: Sketch of the stainless steel capillary test section.



Figure 11: Microchannel used to measure pressure drops.

- if we want to use the configuration B with the mixture, we also turn on the thermostatic bath at the set temperature and open the valve of the compressed air or start the peristaltic pump;
- on the syringe pump we set the type and the volume of syringe;
- we fill a portion of the syringe with the liquid;
- with the help of another syringe, we withdraw the liquid from the bath so that by flowing through the inlet pipe, the test section, and the outlet pipe it removes air bubbles;
- when the syringe begins to fill, we disconnect the tube from the second syringe and connect it to the syringe on the pump;
- we start the pump with a flow rate of 1 ml/min to avoid the presence of air in the syringe;
- we stop the pump;
- on the pump we set the flow rate, that we want to study;
- we check that the pressure drop transducer gives a zero pressure when the pump is stopped;



Figure 12: Counter current pipe in pipe heat exchanger used with the stainless steel capillary.

- we turn on the pump;
- we set the resistance of the connection tube between bath and channel, so that the liquid enters at the desired temperature in the channel;
- when the current through electric temperature of inlet is good and pressure drop becomes constant, we begin the acquisition for 20-30 seconds;
- we stop the pump and verify that the pressure drop is zero;
- we set another flow rate and restart from point 8;
- when the syringe is full of liquid, the syringe is automatically emptied by the pump, pushing the liquid back into the heating bath;
- at the end of the experiment session we empty the channel from the liquid and if the liquid is not water, we use distilled water to clean the channel and the tubes.

The previous steps are repeated for each of the 4 fluids used in each heat exchanger.

2.1.2.3 Water Pressure Drop Measurements in glass channel We studied the pressure drops of water to know the behavior of a well known fluid in the channels: in Fig.13 it is showed that water behavior can be approximated by a straight line in relationship with flow rate.

In the glass channel we tested the flow rate from 0.2 ml/min to 2.5 ml/min with a step of 0.1 ml/min.

So we extracted a relation between the slope of the experimental data and the viscosity of water and we use that piece of information as a geometrical parameter of the micro-channel. In fact, in a laminar flow, pressure drops are a function of the geometry of the channel and of the viscosity, but the geometry is a constant in our experiments.

Because the viscosity is a function of the temperature, we used this formula to calculate water viscosity:

$$\mu(T) = 2.414 \cdot 10^{-5} 10^{\frac{247.8}{T-140}} \text{ Pa} \cdot \text{s} \quad (7)$$

Then the viscosity at 20°C is $\mu = 1.002 \text{ mPa} \cdot \text{s}$.

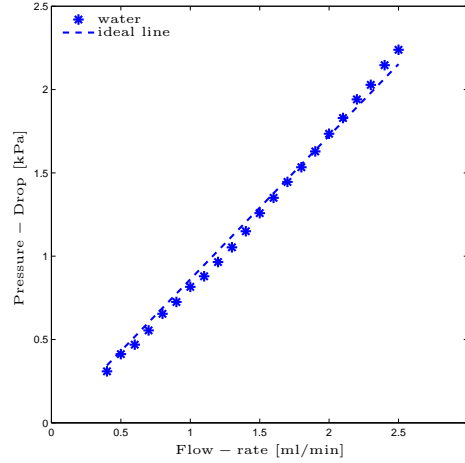


Figure 13: Water Pressure Drop with $T_{\text{inlet}} 30^{\circ}\text{C}$ in the glass test section.

Using the relation 1, we could extract the coefficient of the trend line:

$$m_{\text{water}} = 16\pi^2 \mu I_p^* \frac{L}{A^2} = 0.8611 \text{kPa} \cdot \text{min/ml} \quad (8)$$

and then calculate the geometric constant of the glass channel as:

$$\alpha = \frac{m}{\mu} = \frac{16\pi^2 \mu I_p^* \frac{L}{A^2}}{\mu} = 6.33162 \cdot 10^7 \text{ml}^{-1} \quad (9)$$

Here we can not replace the geometrical parameters because our glass channel has a very high roughness and uncertain geometry and the inlet and outlet plugs form an angle of 90° . However, the linearity between flow-rate and pressure drop is correct.

2.1.2.4 Water Pressure Drop Measurements in stainless steel capillary For the stainless steel capillary we tested the flow rate from 0.05 ml/min to 0.225 ml/min with a step of 0.025 ml/min. In this second experimental set-up the measure on the inner diameter of the pipe is well known ($250 \mu\text{m}$) and the roughness is low.

Using Equation 1 and the same value for the water viscosity the agreement is very good.

The geometric constant of the steel capillary is:

$$\alpha = \frac{m}{\mu} = \frac{16\pi^2 \mu I_p^* \frac{L}{A^2}}{\mu} = 6.33162 \cdot 10^7 \text{ml}^{-1} \quad (10)$$

Fig. 14 shows the difference between the value measured and the value calculated. It is always less than 10%, and the shape is once again linear proving that with a known geometry this correlation works properly.

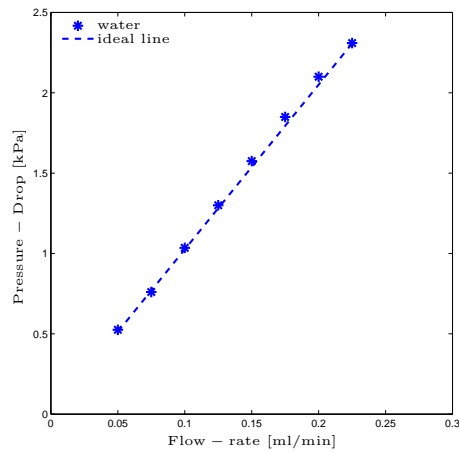


Figure 14: Water Pressure Drop with $T_{\text{inlet}} 30^{\circ}\text{C}$ in the steel capillary.

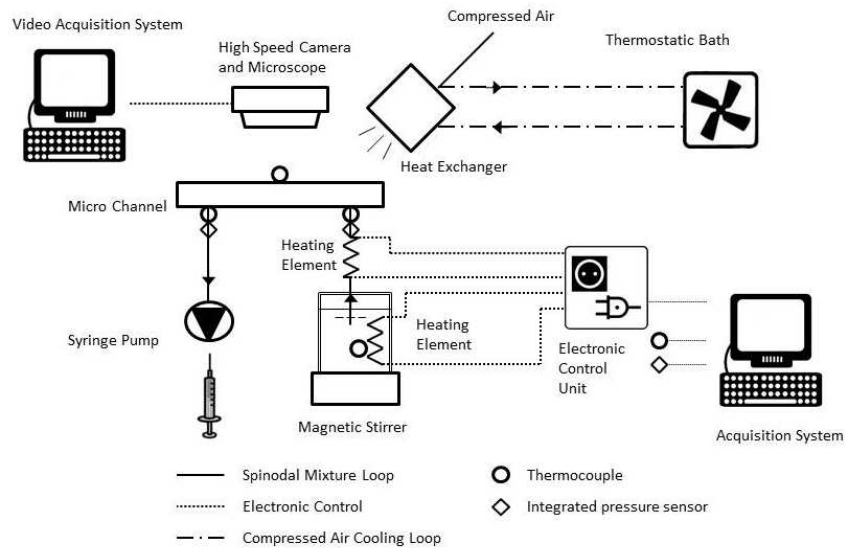


Figure 15: Sketch of the experimental set-up.

2.1.3 Visualizations

2.1.3.1 Visualizations setup In Fig. 15 there is a sketch of the experimental set-up used for the visualization. It is very similar to the glass set-up used for measuring pressure drop, but instead of using a test section made of two microscope glass slides we used one with three slides. The choice of adding an extra microscope slide was made because the roughness of the channel used for measuring the pressure drop was too high to see clearly the spinodal decomposition inside the micro channel. Therefore, as can be seen in Fig. 16 we use three slides: the first, just like for the pressure drop measurements, presents only two circular openings where we paste the inlet and outlet plugs; the second slide, instead of the groove, has a square channel that goes through the whole slide; the third has no machining and is just used for the visualization.

Using air as cooling fluid and a square channel as visualization chamber we have no lens effect that can affect our measure.



Figure 16: Microchannel used to measure pressure drops.

2.1.3.2 Procedure for the visualizations The visualizations are based on the fact that, when homogeneous, each of the two phases is transparent to light: therefore, the passage of the mixture from single-phase to two-phase structure involves the passage from a transparent liquid to one characterized by darker and clearer zones; initially the phases are bicontinuous, then the darker phase forms drops in a clearer background. The visualization procedure is quite simple:

1. the temperature of the mixture is set at 32 °C in the heating bath;
2. we set how long the video recording has to be (usually between 5s and 10s);
3. the microscope camera lens is focused on the desired stretch on the channel;
4. the liquid is drawn into the channel with the maximum flow rate available (30 ml/min with 5ml syringe or with 10ml syringe) to have only mixed mixture in the channel;
5. the flow rate is set at 15 $\mu\text{l}/\text{min}$, so that the liquid begins to flow at low speed in the channel;

6. we start to capture the video with the camera;
7. the mixture undergoes a drastic cooling;
8. a quality control is made on the video to decide if it can be keep or must be discard due to some problem (dust, change in light);
9. we restart from point 2;
10. when we finish the programmed tests we empty the channel from the mixture and use water to clean the channel and the tubes.

Two types of cooling procedure are used: one at room temperature (A configuration), with the slide about 25-26 °C; the other cooled with compressed air (B configuration), microscope resulting in a temperature of the slide around 22-23 °C. The thermostatic bath to cool the plate fin heat exchanger is set at 0°C to obtain these values of cooling.

2.2 Numerical Approach

2.2.1 Synthetic concentration and velocity fields to model transport enhancement effects due to Korteweg micro-agitation during spinodal decomposition

In the final report of AOARD Grant FA2386-10-1-4146, we described two synthetic approaches that consist of two variants, that we called Synthetic Concentration Fluctuation (SCF) and Synthetic Concentration and Velocity Fluctuations (SCVF). In the SCF approach, we substitute the highly non-linear species concentration transport equation (Cahn-Hilliard equation) with a synthetically generated fluctuation field $\phi'(x)$ that retains the well-documented structure and self-similarity features typical of the intermediate stage of spinodal decomposition (SD) of low-viscosity mixtures. The Korteweg body force term in the Navier-Stokes (NS) equation and the excess enthalpy source/sink term in the energy equation are computed at every time step from the synthetic concentration field. In particular, we impose the following structure factor

$$S_{\phi\phi} = \langle \tilde{\phi}(\mathbf{k}) \tilde{\phi}(-\mathbf{k}) \rangle = R^n f(Rk) = A_0 R^n \frac{(CRk)^2}{[1 + (CRk)^2]^3} \quad (11)$$

where \mathbf{k} $k = |\mathbf{k}|$ and n ∇ is the number of dimensions ($n = 3$ for 3D) n , and the dimensionless self-similarity function $f(Rk)$ features (1) a peak at $k \approx 1/R$, where R is the characteristic length scale of the growing domains; (2) a k^{-4} Porod tail as observed in numerical studies ([Kendon *et al.* (1999)], [Kendon *et al.* (2000)]); and (3) a k^2 power law at small k , as prescribed by ([Kendon *et al.* (1999)], [Kendon *et al.* (2000)], [Sain and Grant (2005)]). In figure 17 the structure factor of the concentration is shown for the direct calculation of the Cahn-Hilliard/Navier-Stokes/Energy equation CHNSE. Our procedure for generating the synthetic concentration-fluctuation field $\phi'(x)$ is similar to the artificial turbulence method used in ([Rosales and Meneveau (2006)]) to study the mixing of a passive scalar in a random turbulent field. At every time step we generate a random field $\hat{\epsilon}(k)$ in Fourier space corresponding to a Gaussian random noise field in real space; we multiply $\hat{\epsilon}(k)$ by the scaling factor

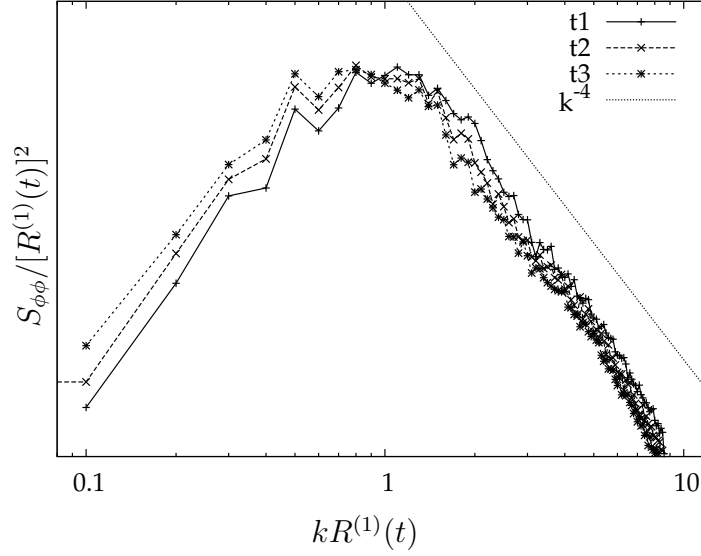


Figure 17: Structure factor of the concentration field obtained from the solution of the full CHNSE model equations normalized over the characteristic length scale of the growing domains.

$\sqrt{R^n f(Rk)}$ to obtain $\hat{\phi}'(k)$; we transform $\hat{\phi}'(k)$ into real space to obtain $\phi'(x)$ which is added to the current concentration field.

In the SCVF approach, we substitute not only the (highly non-linear) momentum transport equation with the synthetically generated fluctuation field $v'(x)$. The procedure for generating the synthetic velocity-fluctuation field $v'(x)$ is different because in order to enforce incompressibility (see again [Rosales and Meneveau (2006)]) after generating the random fields $\hat{e}_i(\mathbf{k})$ in Fourier space corresponding to a Gaussian random noise for each velocity component, we make them divergence free by the projection tensor $P_{ij} = \delta_{ij} - k_i k_j / k^2$, and renormalized. Then we multiply the result by the scaling factor $\sqrt{R^n f(Rk)}$ to obtain $\hat{v}'(x)$ and anti-transform into real space to obtain the fluctuation field $v'(x)$ which is added to the current velocity field.

In the CHNSE simulations the full set of Cahn-Hilliard/Navier-Stokes/Energy equation are solved for a fixed domain. The equations are

$$\frac{D\phi}{Dt} = \frac{D}{RT} \phi(1 - \phi)(\nabla \hat{\mu})_T, \quad \nabla \cdot \mathbf{v} = 0; \quad (12)$$

$$\rho \frac{D\mathbf{v}}{Dt} = -\nabla p + \eta \nabla^2 \mathbf{v} + \mathbf{F}_k, \quad \mathbf{F}_k = -\rho \phi \nabla \hat{\mu} \quad (13)$$

$$\rho M \frac{Dh}{Dt} = k \nabla^2 T + \Phi, \quad \frac{D}{Dt} = \frac{\partial}{\partial t} + \mathbf{v} \cdot \nabla \quad (14)$$

where ρ is the density of the mixture, T the temperature, F_k the body force (also known as Korteweg Force), η the viscosity of the mixture, D the diffusion coefficient, $\hat{\mu}$ the generalized chemical potential, M the molar mass, h the molar

enthalpy, \mathbf{v} the velocity, k the conductivity. Since the Gibbs free energy (g) can be expressed as

$$g = \phi g_{11} + (1 - \phi) g_{22} + RT[\phi \ln \phi + (1 - \phi) \ln(1 - \phi)] + g_{ex} + \frac{M\epsilon}{2\rho} |\nabla \phi|^2 \quad (15)$$

the generalized chemical potential $\hat{\mu}$ as:

$$\hat{\mu} = \frac{\partial g}{\partial \phi} - \nabla \cdot \frac{\partial g}{\partial \nabla \phi} = RT \ln \frac{\phi}{1 - \phi} + \frac{\partial g_{ex}}{\partial \phi} - \frac{M\epsilon}{\rho} \nabla^2 \phi. \quad (16)$$

and the molar enthalpy

$$h = \phi h_{11} + (1 - \phi) h_{22} + h_{ex} + \frac{M\epsilon}{2\rho} |\nabla \phi|^2 \quad (17)$$

In the above model some drastic approximations have been used to simplify the model. Some of these simplifications are: no excess enthalpy (regular mixture), no excess volume, no cross effects (Soret, Dufour), one-parameter Margules model for the non-ideal but regular thermodynamic behavior, constant density, viscosity and thermal conductivity (independent of composition). The two coarse grained approaches (SCF, SCVF) have been tested against the analytical and CHNSE results for the well known problem of thermal diffusion between two semi-infinite domains initially at different temperature suddenly brought into full contact.

3 Results

3.1 Experimental Results

3.1.1 Heat Transfer Enhancement Measurements

To obtain the heat exchanged during phase transition, several experiments were conducted following the experimental procedure outlined in Section 2.1.1.2. The experimental results correspond to various flow rates of the solvent system in the heat exchangers at different inlet temperatures and wall temperatures. The experiments were conducted with pure fluids and with a mixture of critical composition (critical molar composition is $y_c = 0.799$ where $y = y_{acn}$ is the mole fraction of acetone and, of course, $1 - y = y_{hex}$ that of hexadecane) and with pure fluids.

3.1.1.1 Single Channel Figs. 18 and 19 shows the results for the Nusselt number for pure acetone and pure hexadecane, respectively. The points refer to the experimental data, while the line refers to the theoretical correlation.

Even if the Reynolds numbers are always lower than the critical value for the laminar to turbulent transition, we see that the correlation for laminar flows does not work well. This is probably due to the inlet and the outlet hoses being perpendicular to the channel, causing an instability in the first part of the channel which maybe changes the motion from the expected laminar condition. The effect seems more pronounced for acetone (Fig.18) than for water (Fig. 7).

For water we find reasonable agreement with the laminar Stephan correlation for developing laminar flow at constant wall temperature

$$\text{Nu} = 3.657 + \frac{0.0677 ((D/L) \text{Re}_D \text{Pr})^{4/3}}{1 + 0.01 [(D/L) \text{Re}_D \text{Pr}]^{1/3}} \quad (18)$$

For acetone the agreement is reasonable only if we compare with the turbulent Petukhov-Gnielinski correlation proposed in [Gnielinski (1976)]

$$\text{Nu}_D = \frac{(f/8)(\text{Re}_D - 1000)\text{Pr}}{1.00 + 12.7(f/8)^{1/2}(\text{Pr}^{2/3} - 1)} \quad (19)$$

This correlation is good for $0.5 < \text{Pr} < 2000$ and $3000 < \text{Re}_D < 5 \times 10^6$ where for smooth pipes, one should use the following for the friction factor: $f = (0.790 \ln \text{Re}_D - 1.64)^{-2}$. For the single channel, $L = 38\text{mm}$, $D = 0.7\text{mm}$. Notice the difference in Prandtl number, respectively, 6.99, 3.60, 37.02, and 19.36 for water, acetone, hexadecane, and the critical mixture. As we can see from Fig. 19 hexadecane is probably in the laminar-to-turbulent transition regime because neither laminar nor turbulent correlations seem to properly predict the Nusselt number.

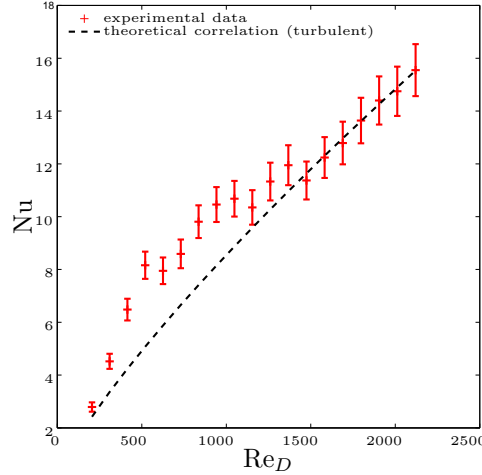


Figure 18: Comparison between theoretical and experimental Nusselt numbers in a single-channel with pure acetone with $T_{\text{bath}}=35^\circ\text{C}$ and $T_{\text{Cu}}=20^\circ\text{C}$.

The first main result for this test section is presented in Fig. 20, where we plot the electrical power absorbed by the resistor during a test made with all our fluids with fixed values of $T_{\text{bath}}=35^\circ\text{C}$ and $T_{\text{Cu}}=25^\circ\text{C}$. These results are interesting because during this test the bulk temperature does not go below the UCST value of 27°C in the channel, so there is no decomposition (except a small region near the walls); without decomposition the properties of the mixture are ideally related only to the properties of its constituents. This test demonstrates that the power absorbed with pure acetone, pure hexadecane, and the mixture with critical composition is almost the same.

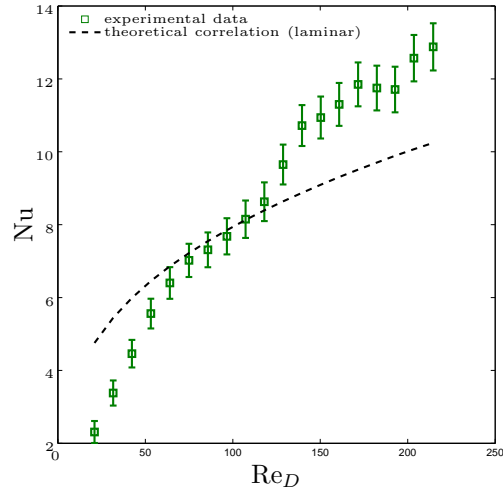


Figure 19: Comparison between theoretical and experimental Nusselt numbers in a single-channel with pure hexadecane with $T_{\text{bath}}=35^{\circ}\text{C}$ and $T_{\text{Cu}}=20^{\circ}\text{C}$.

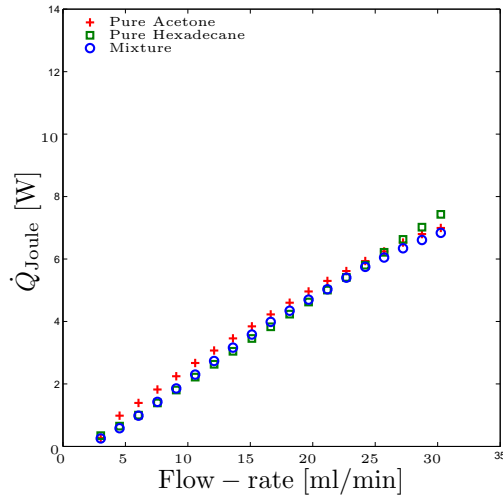


Figure 20: Absorbed electrical power versus flow-rate with $T_{\text{bath}}=35^{\circ}\text{C}$ and $T_{\text{Cu}}=25^{\circ}\text{C}$, measured for single channel flow of pure acetone, pure hexadecane, and a mixture of acetone and hexadecane with critical mole fraction ($y_{\text{acn}} = 0.799$). Mixture data and pure-component data show no important difference since spinodal decomposition occurs mildish for $T_{\text{Cu}}=25^{\circ}\text{C}$.

Then we imposed a lower temperature on the heat exchanger ($T_{\text{bath}}=35^\circ\text{C}$ and $T_{\text{Cu}}=20^\circ\text{C}$) and we estimated the theoretical Nusselt number for laminar flow using Eq.6 and assuming that all the mixture thermo-physical properties, except the specific heat, are based on a mass average of the values of the pure fluids. The specific heat of the mixture has been measured with a Differential Scanning Calorimeter and resulted in $c_p = 2230 \text{ J}/(\text{kg K})$. Fig. 21 shows that the experimental Nusselt number is almost a factor of 2 higher than the theoretical correlation would predict. We take this as a demonstration of the enhancement due to micro-agitation induced by spinodal decomposition.

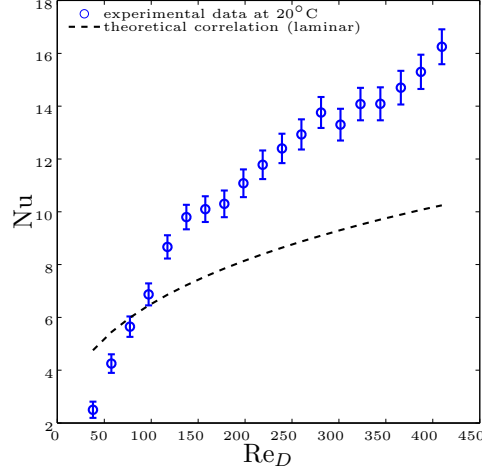


Figure 21: Comparison between theoretical and experimental Nusselt numbers in a single-channel with a critical mixture of acetone and hexadecane, $T_{\text{bath}}=35^\circ\text{C}$ and $T_{\text{Cu}}=20^\circ\text{C}$. Here the quench is deep enough that spinodal decomposition induces a heat transfer enhancement, except for the first five experimental point at low flow rates (that we report for completeness, but may be affected by large errors, see section 2.1.1.3.2).

This is the second main result with the single channel test section. Similarly to Fig.20, Fig.22 shows the measured value of \dot{Q}_{Joule} versus the flow rate obtained with $T_{\text{bath}}=35^\circ\text{C}$ and $T_{\text{Cu}}=20^\circ\text{C}$ for pure acetone, pure hexadecane, and the critical mixture.

3.1.1.2 Multichannel As for the single channel, we tested the multichannel exchangers with the same two quench temperatures of 25°C and 20°C . With 25°C , our visualization, shows a mild spinodal decomposition; with 20°C , instead, the quench is deep enough that we do observe vigorous spinodal decomposition in the section. Figs. 23 to 26 show the heat exchanged by the pure fluids and the critical mixture.

To evaluate the enhancement effect, we compute the Augmentation Factor AF defined as follows:

$$\text{AF} = \frac{\dot{Q}_{\text{Joule}}^{\leftarrow} - \dot{Q}_{\text{Joule}}^{\leftarrow} \big|_{\text{mix without decomposition}}}{\dot{Q}_{\text{Joule}}^{\leftarrow} \big|_{\text{mix without decomposition}}} \quad (20)$$

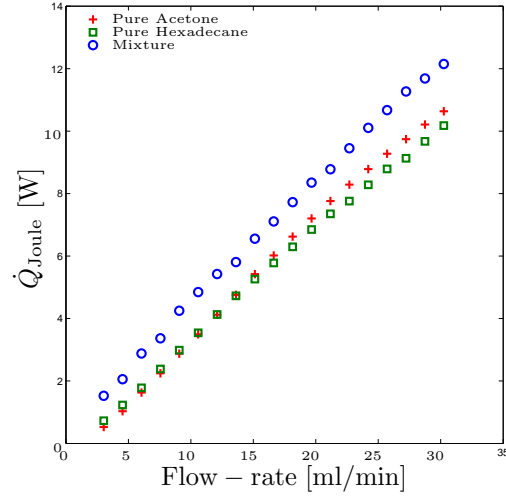


Figure 22: Absorbed electrical power versus flow rate measured for single channel flow with $T_{\text{bath}}=35^{\circ}\text{C}$ and $T_{\text{Cu}}=20^{\circ}\text{C}$. Compared with Fig. 20 the data for the mixture show enhanced heat transfer as expected since vigorous spinodal decomposition does occur for $T_{\text{Cu}}=20^{\circ}\text{C}$.

where $\dot{Q}_{\text{Joule}}^{\leftarrow}$ is the measured electrical power absorbed by the hot-reservoir resistor for the actual flow conditions, and $\dot{Q}_{\text{Joule}}^{\leftarrow} \big|_{\text{mix without decomposition}}$ is assumed to be equal to the average of $\dot{Q}_{\text{Joule}}^{\leftarrow} \big|_{\text{pure acetone}}$ and $\dot{Q}_{\text{Joule}}^{\leftarrow} \big|_{\text{pure hexadecane}}$ measured at the same flow rate. This assumption is justified by the data of Fig. 20 which show that in absence of decomposition the mixture and the two pure components yield approximately the same $\dot{Q}_{\text{Joule}}^{\leftarrow}$ for the same flow rate.

The correlation between the augmentation factor defined in Eq. 20 with AF_{id} defined in [Di Fede *et al.* (2011)] will be discussed elsewhere.

Fig. 27 is made using the data of Figs. 23 to 26. It shows that the performance increase is greater at lower flow rate. This is because there is a sort of summation of the effects: the more is the heat exchanged because of the increase of flow rate the less is the heat exchanged due to the spinodal decomposition induced convection.

The augmentation factor is higher in the multi-channel heat exchangers. This is due to the fact that the tests were conducted under the same flow rates in the two cases, but in the multi channel heat exchangers the flow rate in every single channel is less than the nominal one. Therefore the fluid velocity is smaller and the effect of the induced convection is greater.

3.2 Spinodal decomposition visualization

Comparing Fig. 23 with Fig. 25 and Fig. 24 with Fig. 26 shows that the enhancement effect is higher for the deep quench (7°C in Figs. 25 and 26, 2°C in Figs. 23 and 24). This is also confirmed by visualizations in single channel setup.

Fig. 28 represents the same piece of channel with constant flow rate (flow

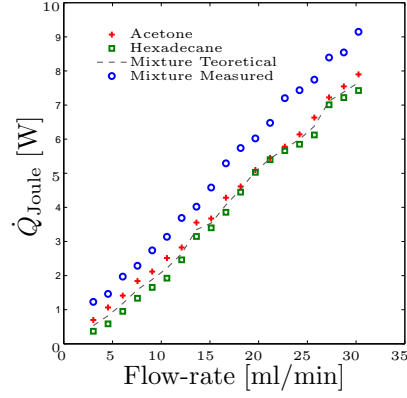


Figure 23: Electric power absorbed by the parallel heat exchanger with $T_{\text{bath}}=35^{\circ}\text{C}$ and $T_{\text{Cu}}=25^{\circ}\text{C}$, 2°C quench mild decomposition.

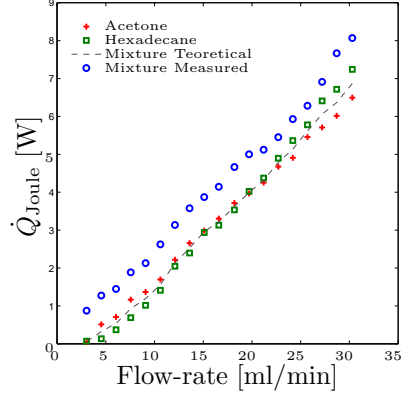


Figure 24: Electric power absorbed for the U-shape heat exchanger with $T_{\text{bath}}=35^{\circ}\text{C}$ and $T_{\text{Cu}}=25^{\circ}\text{C}$, 2°C quench mild decomposition.

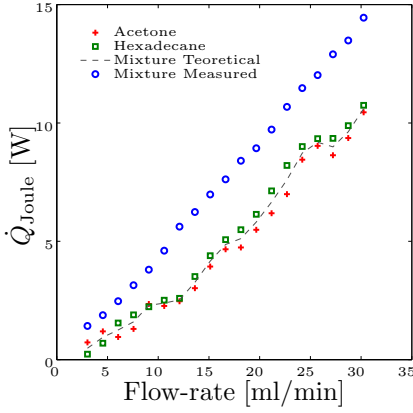


Figure 25: Electric power absorbed by the parallel heat exchanger with $T_{\text{bath}}=35^{\circ}\text{C}$ and $T_{\text{Cu}}=20^{\circ}\text{C}$, 7°C quench vigorous decomposition.

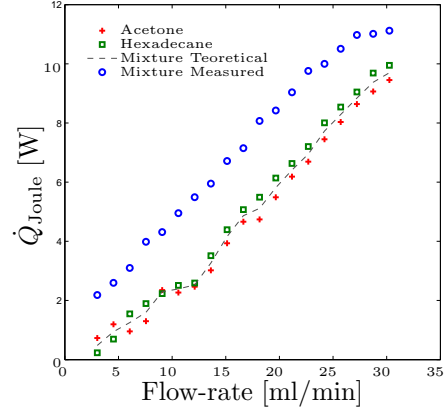


Figure 26: Electric power absorbed for the U-shape heat exchanger with $T_{\text{bath}}=35^{\circ}\text{C}$ and $T_{\text{Cu}}=20^{\circ}\text{C}$, 7°C quench vigorous decomposition.

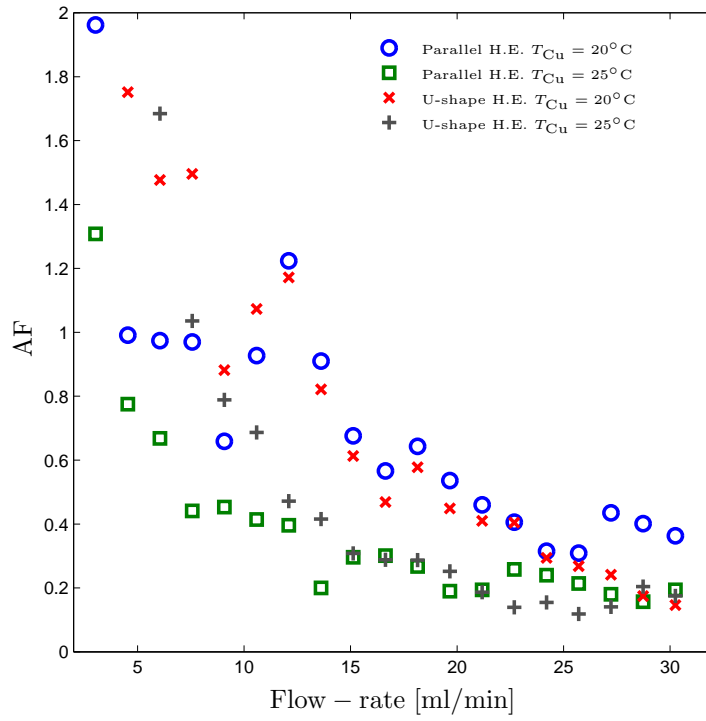


Figure 27: Heat-transfer Augmentation Factor (AF) as defined by 20, computed from the data in Figs. 23 to 26.

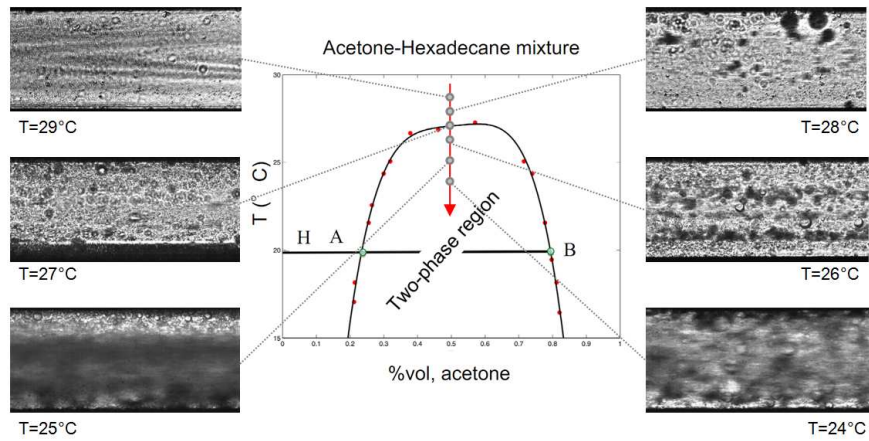


Figure 28: Effect of quench depth on the vigorousness of the spinodal decomposition of an acetone-hexadecane mixture in a single-channel flow.

rate was set to the lower value possible for our set-up – 1.5 ml/min – to take better pictures) at different T_{Cu} temperatures. We can see that there are two types of flow. At higher temperatures (above the spinodal region) we see the presence of relatively large bubbles; these are probably due to the fact that a little decomposition can be induced by shear in the pipe. At lower temperatures (under the spinodal curve) there is the formation in situ of a large number of micro-droplets that induce convective motion because of the difference in composition of the two phases. Both effects increase the heat transfer, but the second in much more vigorous way.

3.3 Pressure Drop Measurement

3.3.0.3 Glass channel We measured the pressure drops in the glass channel following the procedure described previously. We started measuring the pressure drop of pure liquids: acetone and hexadecane. The fluids came in micro channel at a temperature of 30°C and were cooled to room temperature by set-up configuration 1. We tested different flow rates from 0.2 ml/min to 2.5 ml/min to study the relationship between flow rate and pressure drop. The results (see Fig.29) show how these two parameters are linearly related.

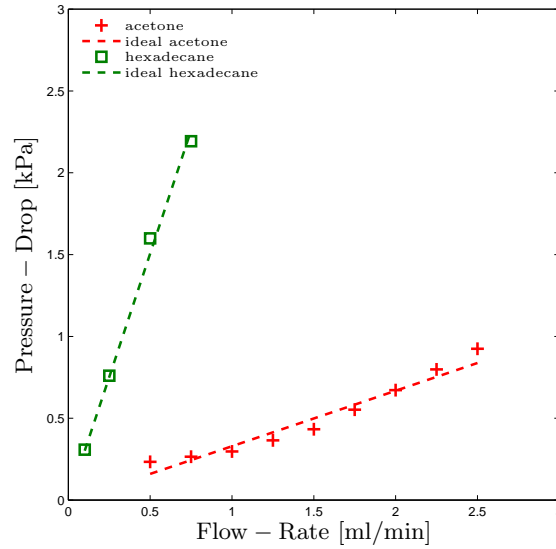


Figure 29: Ideal and real behavior of acetone and hexadecane in the micro-channel

We calculated the viscosity from these relations:

$$\mu_{acetone}(T) = \exp(-3.37955 + \frac{553.4}{-46.97 + T}) \text{ mPa} \cdot \text{s} \quad (21)$$

$$\mu_{hexadecane}(T) = \exp(-4.0453 + \frac{1247.3}{-55.86 + T}) \text{ mPa} \cdot \text{s} \quad (22)$$

We made the average between the inlet and outlet temperatures of the fluids during our tests and we found that

$$\mu_{acetone} = 0.30 \text{ mPa} \cdot \text{s} \quad (23)$$

$$\mu_{hexadecane} = 2.88 \text{ mPa} \cdot \text{s} \quad (24)$$

So we were able to calculate the ideal behavior of these two liquids (Fig.29) on the graph flow-rate/pressure drop by the constant of the channel obtained from water tests

$$m_{acetone} = \alpha \cdot \mu_{acetone} = 0.32 \text{ mPa} \cdot \text{s} \quad (25)$$

$$m_{hexadecane} = \alpha \cdot \mu_{hexadecane} = 3.04 \text{ mPa} \cdot \text{s} \quad (26)$$

Next, we analyzed the mixture, for which there are no models of behavior in literature. Initially, we calculated an ideal viscosity for the mixture with a literature model(27):

$$\mu_{mixture} = 0.799\mu_{acetone} + 0.201\mu_{hexadecane} = 0.82 \text{ mPa} \cdot \text{s} \quad (27)$$

After these theoretical considerations, we started tests analyzing the mixture at room temperature of 25°C and conditions whereby it remains mixed through the channel. The pressure drops at low flow rate are near to ideal straight line (Fig.30).

Then we studied the mixture mono-phase, with an inlet temperature of 30°C and outlet greater than 28°C. Also in this case the mixture was completely mixed at the end of the channel (Fig.30).

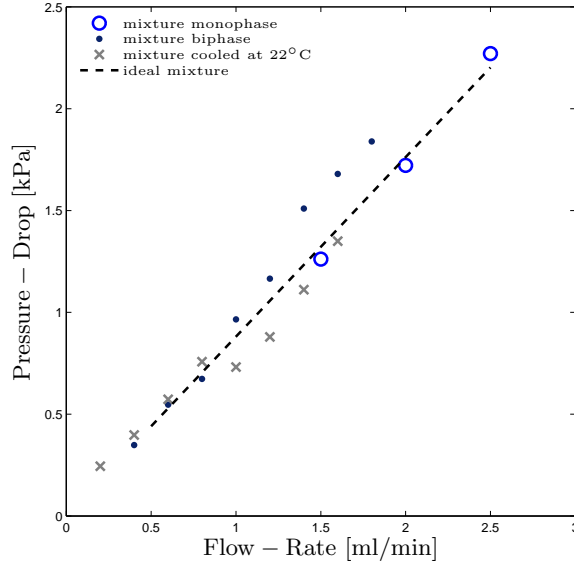


Figure 30: Mixture at room temperature

Finally, we analyzed the mixture with inlet temperature of 30°C and with a cooling of 22°C obtained with the use of the thermostatic bath. The data

show that with this cooling conditions, the pressure drop follows that of the mixture at room temperature down to a flow rate between 0.8 ml/min and 1 ml/min. At lower flow rates, the pressure drop is greater than that at 1 ml/min. The experiments have been repeated several times and this behavior has been confirmed. At this stage we have not identified yet a convincing explanation of the reason for this behavior of the pressure drop in this particular range of flow rates. After this discontinuity, the pressure drop tends to return towards the ideal behavior for higher flow rates.

3.3.0.4 Stainless steel capillary As can be seen from the Fig.31 the pressure drops of pure acetone and of pure hexadecane follow almost perfectly the correlation expressed in the previous section. The small variations, in particular for what concerns acetone, can be traced back to an insufficient degree of purity (we used an acetone at 95 % purity) and to an incorrectly calculated viscosity as well.

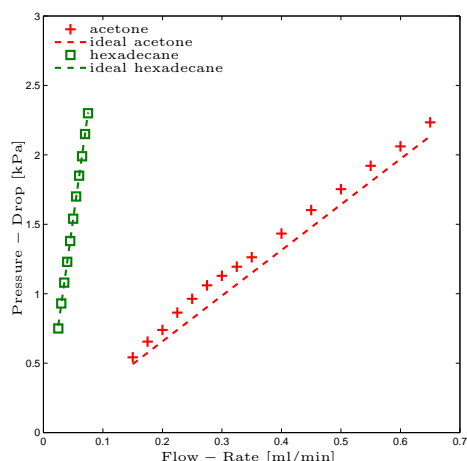


Figure 31: Ideal and real behavior of acetone and hexadecane in the micro-channel

For what concerns the pressure drop of the spinodal mixture it can be noted that, as in the previous case, when the mixture is single phase (fully mixed above 27°C) the pressure losses are very similar to those calculated with the theoretical correlation. Yet in a similar manner to the case with the glass channel the pressure drop of the mixture cooled to 22°C, are significantly below those of the completely mixed mixture.

The test with the stainless steel capillary, however, differs from the one with the glass channel for what concerns the pressure drop of the two-phase non demixing flow (the two-phase flow enters the test section at 25°C and exits at the same temperature).

In the latter case the pressure drops are even lower than those that occur with the mixture during the decomposition. We believe that the difference between these two behaviors is mostly due to the affinity of either phase with the conducting wall.

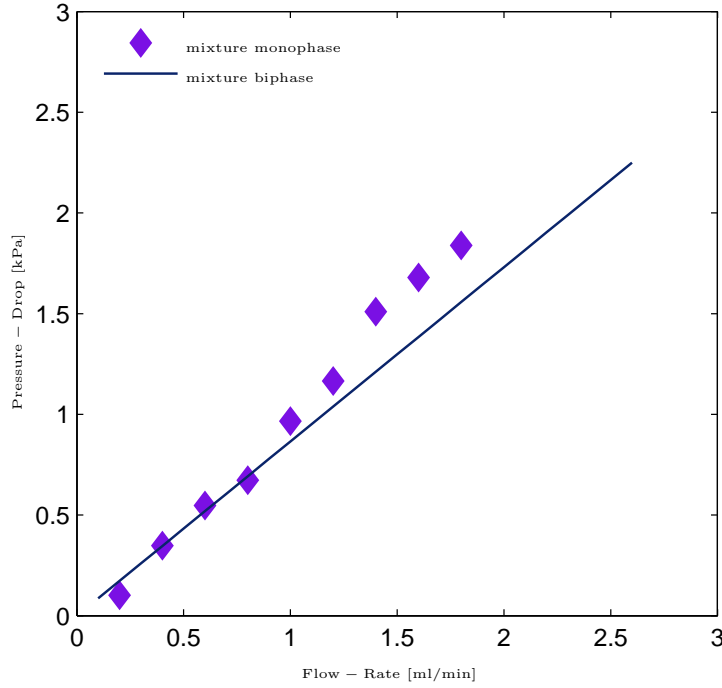


Figure 32: Mixture at room temperature

Further evidence relating to the contact angle and the pressure losses in ducts of larger diameter showed that the phase rich in hexadecane (therefore the more viscous) is closer to the glass. The acetone-rich-phase is closer to the stainless steel, instead.

These results will be the topic of an ad-hoc publication, since they need to be further investigated and are very important from the applications point of view.

3.4 Visualizations

We worked on different videos at different magnification (100X and 200X) and we used two different kind of post processing: a PTV-like algorithm and a PIV-like post processing.

3.4.1 PTV-like post processing

The videos helped us to better understand how the spinodal decomposition occurs. We acquired two videos at 100X: one with subcooling at 25°C (Fig.34), the other with a subcooling at 21°C (Fig.33).

In the first video we could see that the spinodal decomposition starts at the edges of the channel (Fig.34(a),34(b)), and then propagate towards the center to occupy the entire channel (Fig.34(c)). Then the phases start to grow, joining together and changing their composition (Fig.34(d),34(e),34(f)).

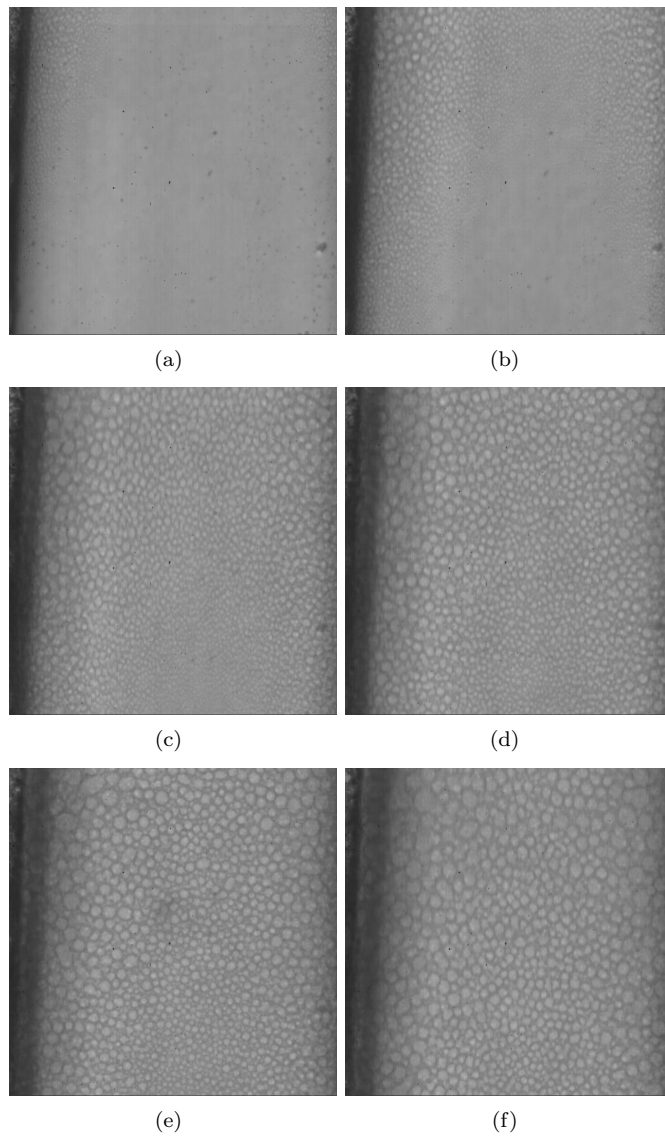


Figure 33: Sequence of spinodal decomposition at 22°C

In the second video one of the most interesting things to notice is the temperature gradient induced by the cooling channel configuration B (Fig. 15), that leads to the formation of phases first at the top-left of the channel (air cooling side) (Fig.33(a)). Then the mixture decomposes in the whole channel, first in bicontinuous way (Fig.33(c)) then with bubbles that grow (Fig.33(e),33(f)).

The videos were analyzed with MatLab to extract trends in overall interfacial area and propagation of the phase during demixing. First the frames were cleaned (Fig.35): the program worked well for both the binarization of the image (Fig. 35(b)) and for the detection of the centers (Fig. 35(f)).

We derived the time evolution of the areas for both videos (Fig.36). We can see that cooling at room temperature the phases swell larger than in the other test.

Next we performed PTV on phases of the first video to see what kind of motion there was in the channel during the decomposition. The program worked very well on the frames in which the decomposition has already developed around the channel and gave us evidence that the motion really passes from laminar of pure fluid to turbulent during this phenomenon.

We also isolated two droplets during the spinodal decomposition in the first video. We took the frames at the final stage of decomposition, where the bubbles were better defined. We followed backwards these bubbles to see how they moved and how their interfacial area evolved (Fig.39). We detected the centers of the phases with the program that we already described. To isolate the phases we started from Sobel-filtered images and we colored the interested phases in red: then we subtracted the red layer from the other layers with MatLab to keep only the colored bubbles (Fig.40).

For this series of images we tracked the center of the phases to calculate the speed (Fig.41(a)) and we measured the growth of the areas (Fig.41(b)). We noticed that the speed tends to increase slightly when phases come together in a single bubble and that there are jumps in speed due to the syringe pump.

For what concern the interfacial areas we already saw that on average they grow over time (Fig.36).

3.4.2 PIV-like post processing

The post processing on the videos with the PTV-like algorithm is so difficult as to make the work very slow and operator dependent. We have therefore chosen to use a PIV-like approach: we use a PIV algorithms (designed for the usual PIV image) for the analysis of our videos. In this way we do not need to binarize every frame (with lots of threshold problems), but we exploit the cross-correlation algorithms implemented in the PIV code to measure how the interface between the phases move.

The work is not yet finished, but we compared the result of the same videos analyzed with the two different algorithms, and the results are very similar, this makes us quite confident about the correctness of the final result.

In Fig. 42 we can see a velocity field generated with the PIV-like technique after an analysis of the velocity profile is clear that we are facing a turbulent flow.

By analyzing a lot of frames we were able to derive sufficient data to perform statistical analysis and obtain a turbulence spectrum.

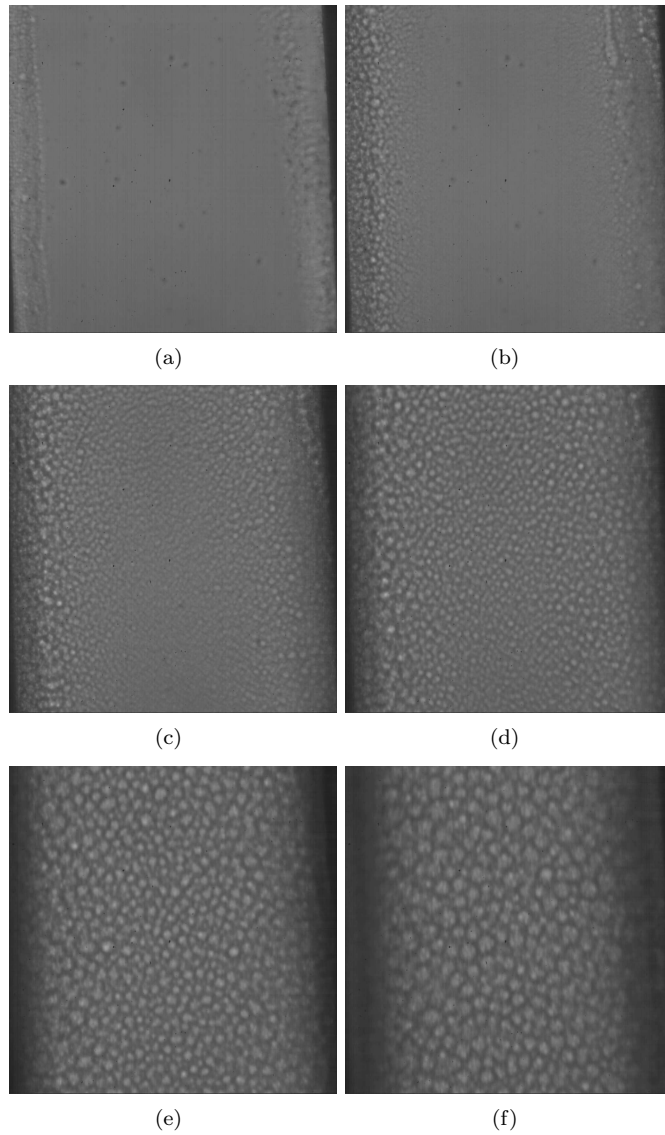


Figure 34: Sequence of spinodal decomposition at room temperature

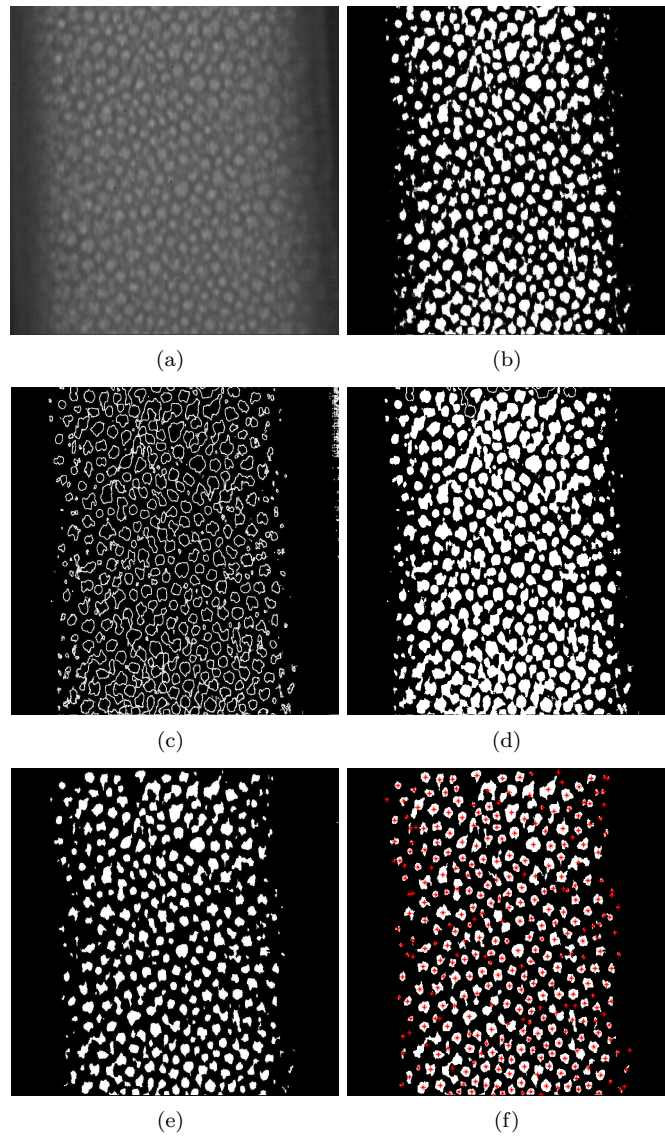


Figure 35: Cleaning of the frames

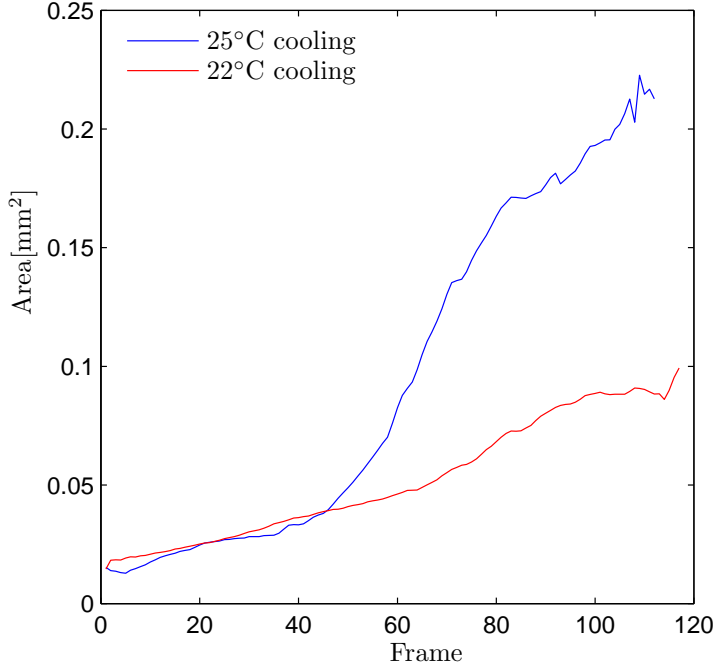


Figure 36: Phase Growth

We note that the trend of the spectra is the same for both the numeric analysis and for the experimental ones.

3.5 Numerical Results

To validate the methods described in section 2.2.1, we compare the results with those obtained with a full CHNSE simulation code based on a staggered finite difference spatial discretization and on a semi-implicit algorithm for time discretization, run on the IBM-SP6 parallel machine available at CINECA with grid size up to 256^3 and fully periodic boundary conditions. In this case the CHNSE temperature profile shows an increase of the heat transfer due to the presence of the convective motion that arises during the formation of the domains in spinodal decomposition. This enhancement is proven in Fig. 45 by comparison with the result known for the same configuration in the absence of decomposition. It is clear from Figure 46 and 47 that the two coarse grained models seem not to be able to predict the same heat transfer enhancement effect. As in turbulence, where reproducing only the spectra of the velocity is not enough to correctly describe all turbulence features at all the scales, also in spinodal decomposition it appears that reproducing only the structure factor behaviour seems to be not enough to characterize the phenomenon.

3.5.0.1 Structure factors for cross-correlation effects For the reasons expressed in the preceding section, we are currently investigating the possibility

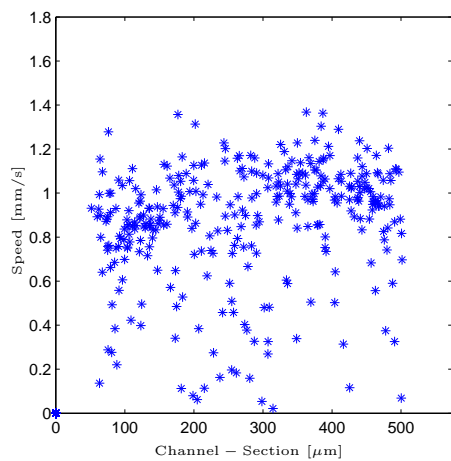
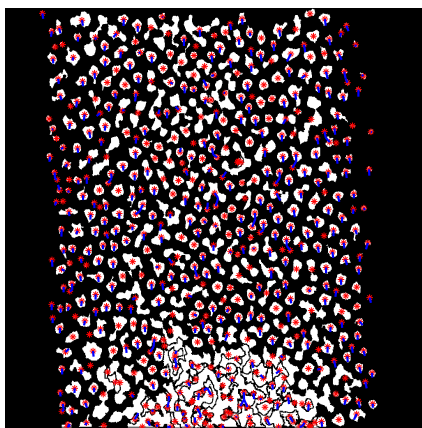


Figure 37: PTV frame 1

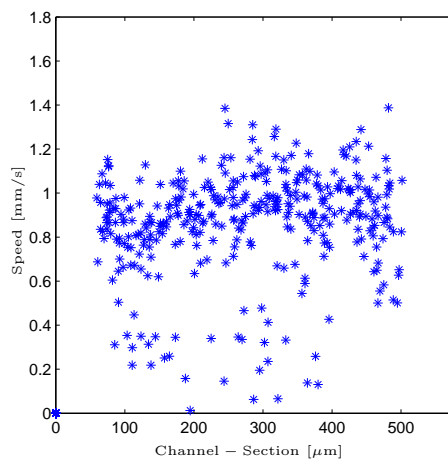
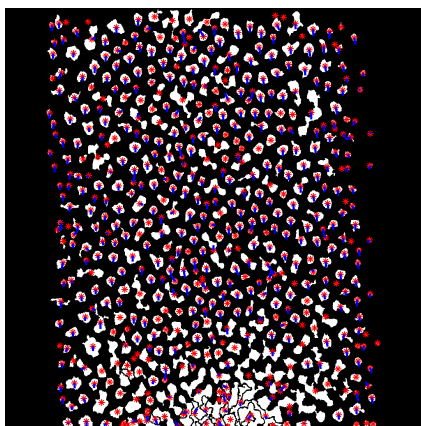


Figure 38: PTV frame 2

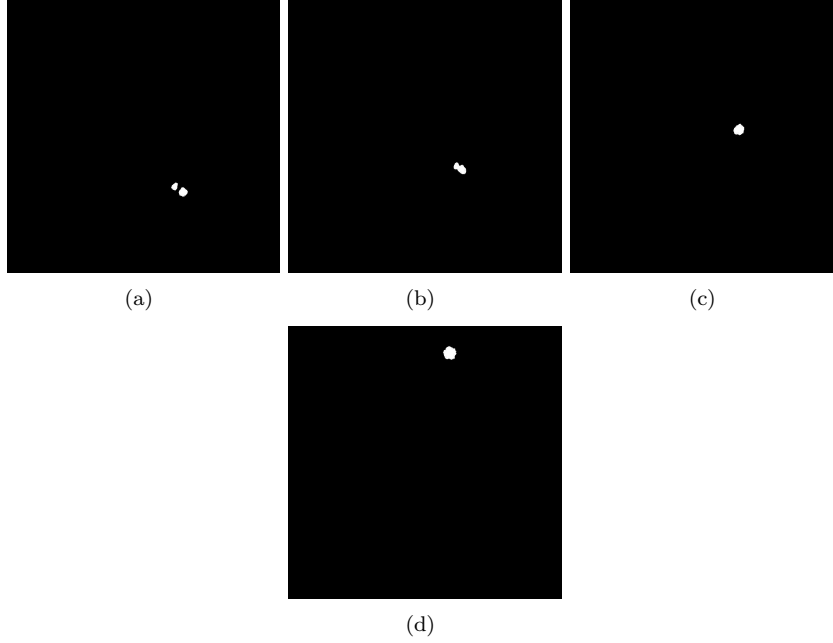


Figure 39: Sequence of isolated phases

of constructing a concentration or a velocity field in which not only the structure factor is reproduced correctly but also other higher order statistics are correctly reproduced. For this reason we decided to extract from the fully coupled CHNSE system the behavior of the cross correlation between the velocity and the temperature and the velocity and the concentration, and the behavior of the Korteweg Force structure factor.

The following are results of very expensive and long simulations that to our knowledge have not been done before, and that we will soon submit for publication. In Figure 48 the structure factor for the structure factor of the cross correlation between velocity and concentration is shown for different times for a selected Peclet number of 1000. The structure factor shows a k^{-6} behavior for the small scales.

In Figure 49 the structure factor for the cross correlation between velocity and temperature is shown for different times for a selected Peclet number.

In Figure 50 the structure factor for the Korteweg force is shown for different Peclet numbers and for different time scales. The k^4 behavior for high k numbers, implies the existence of strong correlations at small scales, as opposed to a non correlated force for small k (bigger scales). This means that the Korteweg force is a local effect strongly correlated to the microscale, in particular the maximum value of the structure factor is found at the interface width.

We meant to continue this line of search by deriving an algebraic equation capable to reproduce the structure factor of the Korteweg force. This equation would then be integrated in the SCF and in the SCVF methods to understand if reproducing the body force that is responsible for the agitation inside the mixture during the spinodal decomposition is enough to reproduce its macro-effect (the heat transfer enhancement). In addition to what has been previously

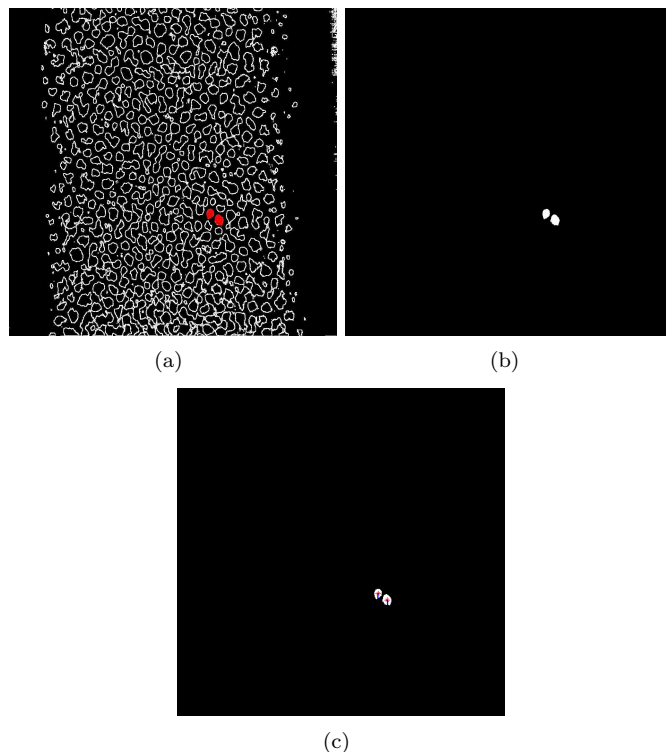
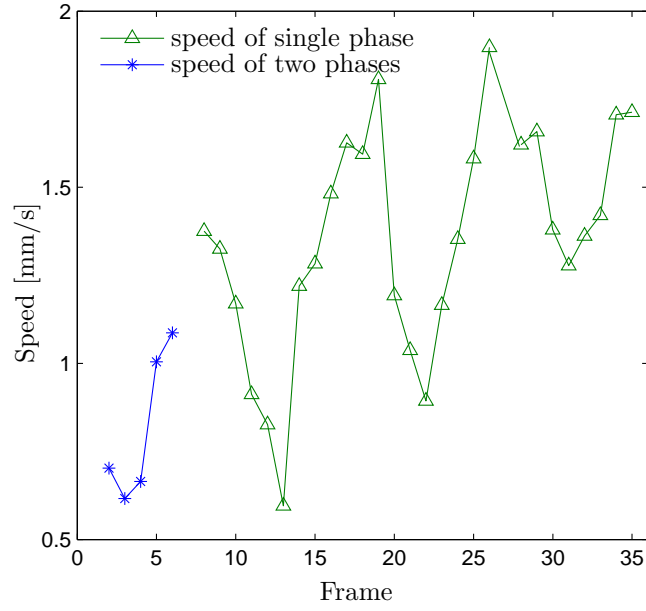


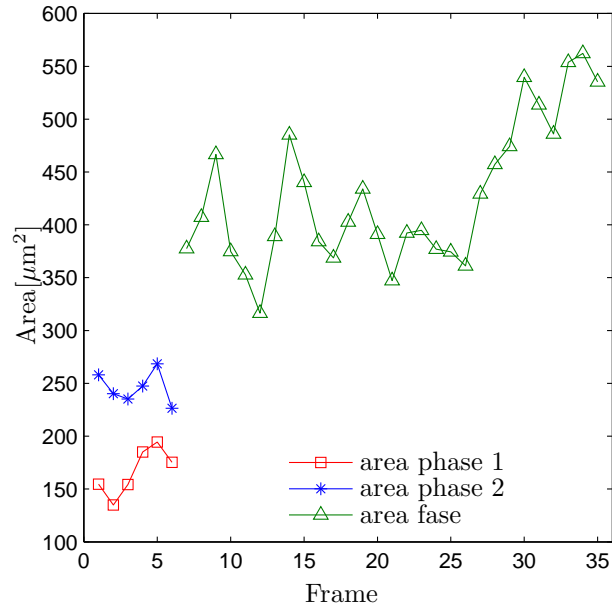
Figure 40: Cleaning of the frames

mentioned, we planned also to extend our simulation with the full CHNSE system to study the behavior of the Korteweg structure factor near the interface. As it shown in Fig. 50 we expected the function to have a maximum around the interface thickness, where the capillary forces are stronger, and then a decreasing as we approach the molecular level.

However, we discontinued this line of research because the post-doc (Dr. Molin) who was the dedicated and expert person on this topic resigned in November 2011. She was replaced after a couple of months by a new beginning PhD student (Neri) who was dedicated to support Farisè in the experimental effort both because training on the numerical aspects would have been impossible in only a few months and because the experimental work was giving more interesting results.



(a)



(b)

Figure 41: Speed and growth of the phases

4 Conclusions

In this Final Report we present a set of experimental and numerical data on heat transfer enhancement due to spinodal decomposition in single and



Figure 42: Image post-processed with the PIV algorithm

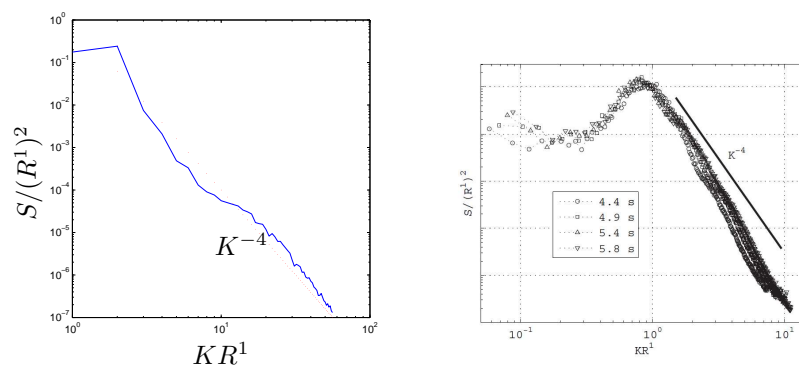


Figure 43: Turbulence spectrum (EXPERIMENTAL)

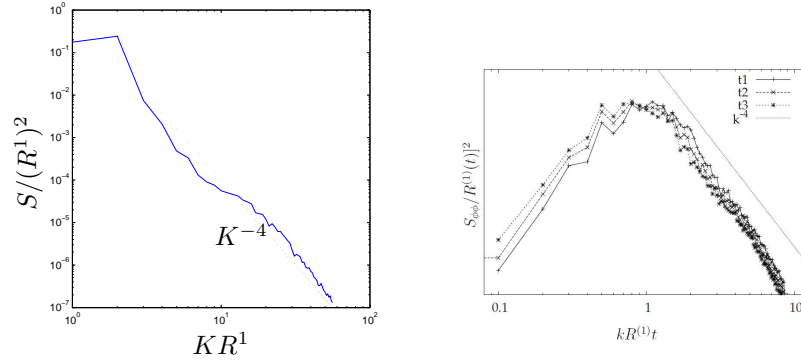


Figure 44: Turbulence spectrum (EXPERIMENTAL/NUMERICAL)

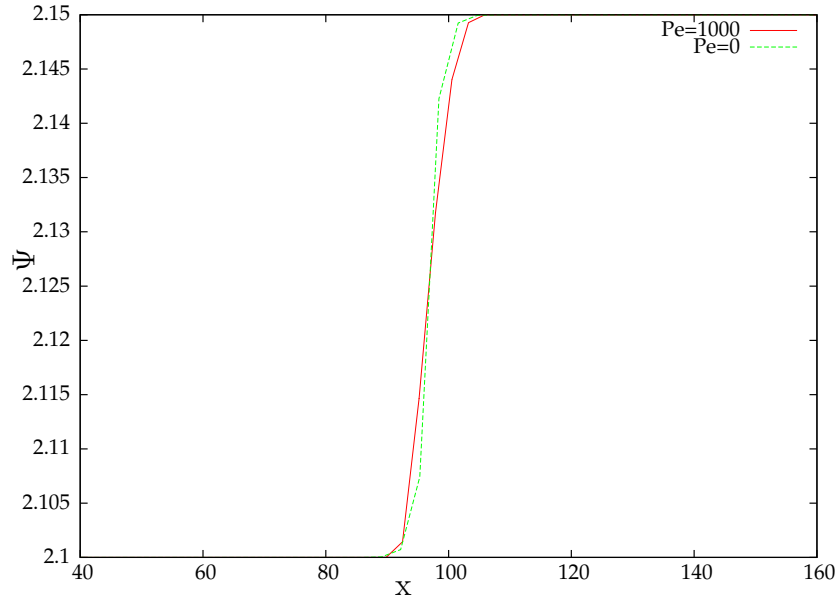


Figure 45: Comparison of the Margules parameter (where $\Psi = \frac{2T}{T_c}$) profile of the DNS calculation for $Pe=1000$ with the analytical profile with no convection ($Pe=0$) at one selected time step

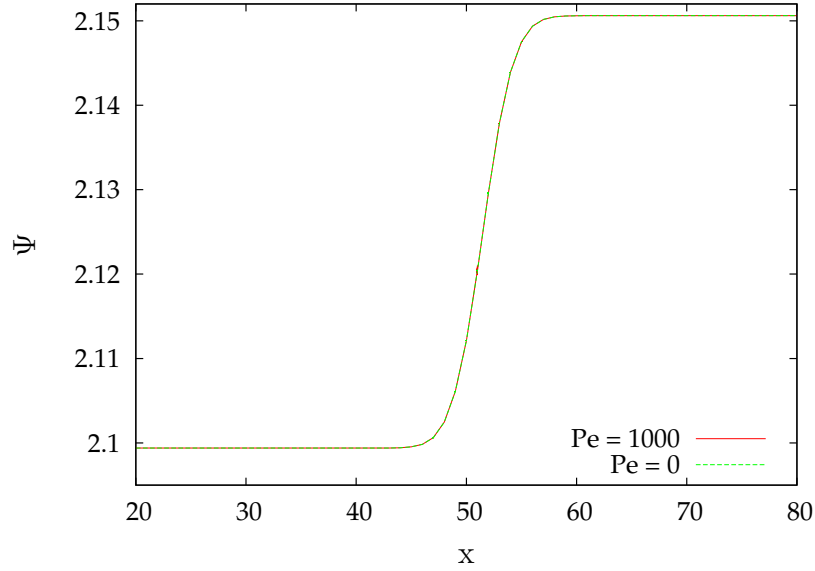


Figure 46: Comparison between the Margules parameter profiles (where $\Psi = \frac{2T}{T_c}$) of the SCVF approach and $Pe=1000$ and of the analytical profile with no convection ($Pe=0$) at one selected time step

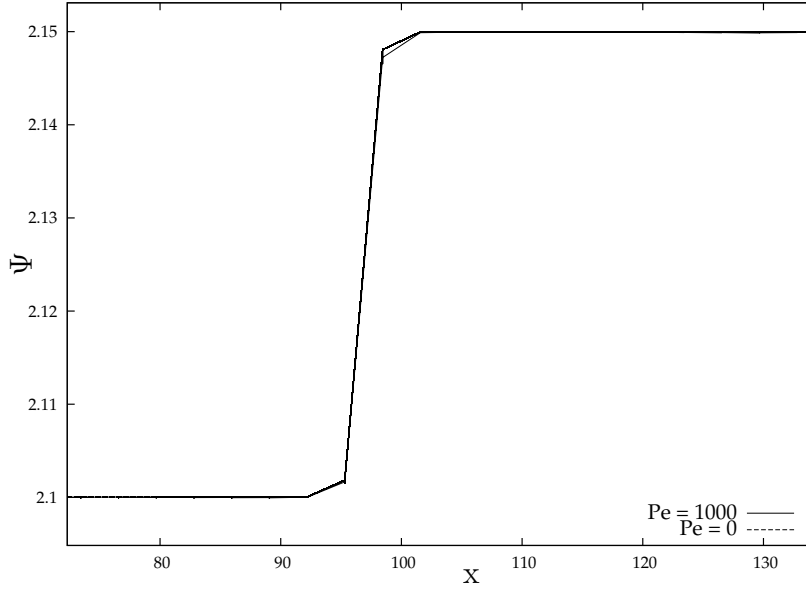


Figure 47: Comparison between the Margules parameter (where $\Psi = \frac{2T}{T_c}$) profiles of the SCVF approach and $Pe=1000$ and of the analytical profile with no convection ($Pe=0$) at one selected time step

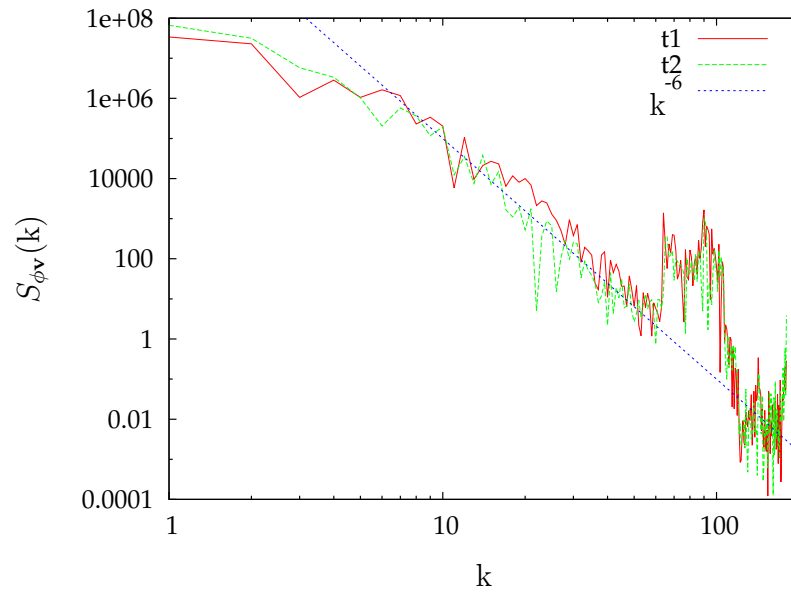


Figure 48: Behavior of structure factor for the cross correlation of concentration and velocity

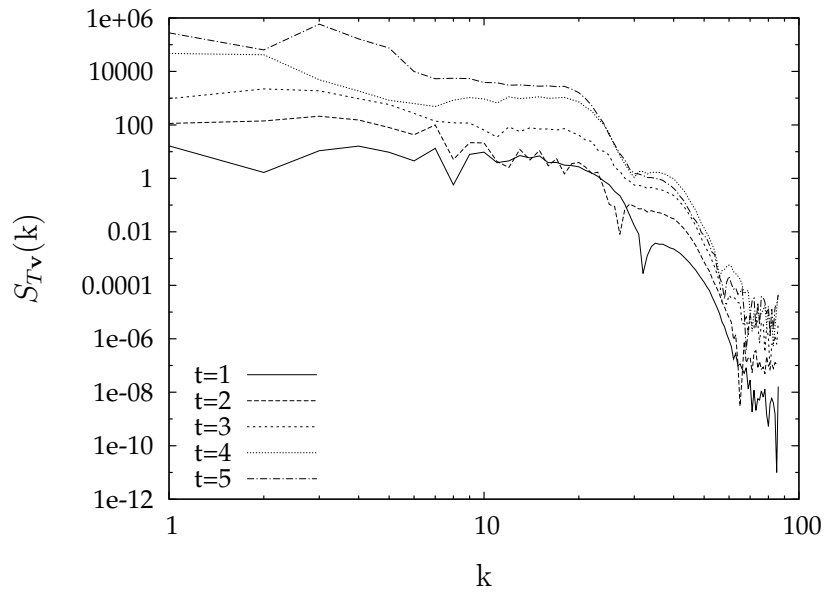


Figure 49: Behavior of structure factor for the cross correlation of temperature and velocity

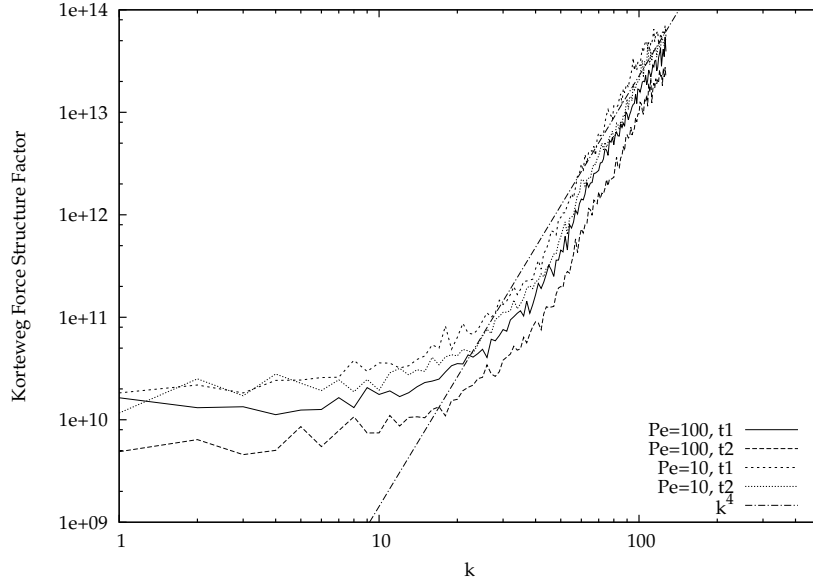


Figure 50: Behavior of the Korteweg force structure factor for two different Peclet number and for different times

multi channel heat exchangers. The values of the simplified augmentation factor defined here are higher than those presented in [Di Fede *et al.* (2011)] ($AF_{id} \approx 0.2 \div 0.4$) obtained with a larger heat exchanger, but lower than those presented in [Poesio *et al.* (2007)] ($AF_{id} \approx 10$) obtained with fluid at rest).

As is shown in Fig.27 the behavior of AF seems to follow exactly the trend outlined in these previous papers and support our conclusion that, as expected, the augmentation factor increases as the size of the channels and the flow rate are decreased. From the point of view of applications, this is an important conclusion because small sizes and low flow rates are typically characterized by small Nu numbers and can therefore benefit most from the spinodal enhancement effect.

Furthermore we measured a slight decrease in the pressure drop, in particular when the flow is decomposing. This is extremely encouraging since all other technology for increasing the heat exchange (ebullition, nanofluids, ...) result in an increase of the pumping power needed.

4.1 Future Developments

In the past few months we started to work with water-triethylamine mixture. We peek this new mixture among several other because it has a lot of appealing features: first of all this pair of fluids have a phase diagram that present an LCST (Lower Critical Solution Temperature) this means that the mixture decomposes itself when we heat it, therefore, it is suitable for cooling applications; secondly the presence of water in the mixture allow us to have very good heat exchange properties (high heat capacity, high heat of vaporization and relatively low viscosity); the phase diagram of this mixture is very flat, therefore, we are going to have good performance for a wide range of relative composition

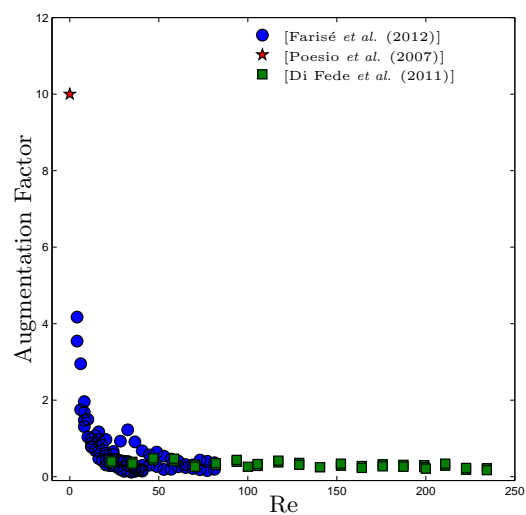


Figure 51: Heat-transfer Augmentation Factor vs Re.

of constituents and we can have spinodal decomposition for concentrations of triethylamine as low as 5-10% in weight; the triethylamine is a relatively safe fluid to work with.

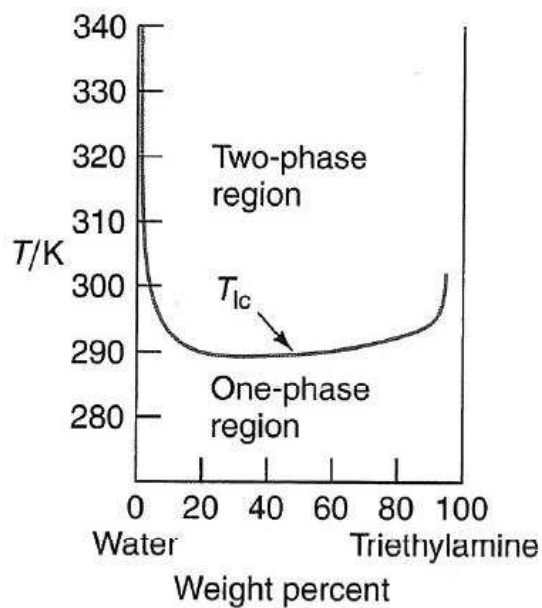


Figure 52: Water and Triethylamine mixture Phase Diagram

We already built the experimental set-up and we are validating it with water.

In the future we will try to combine the technologies of spinodal decomposition and phase change. This new combination appears to be particularly promising when we will work with multi-component mixtures where only one phase changes its state from liquid to gas and the other phase is closer to the wall. In this way it would be possible to almost completely eliminate the problem of dry-out and one could take full advantage of the latent heat of evaporation.

We hope that EOARD finds this developments interesting and will offer further support. In the meantime, we are grateful for the support given so far and we are certain that the wealth of experimental and numerical results produced by this project has been perceived as satisfactory.

4.2 Articles and Conference Proceedings Produced So Far and Acknowledging this Grant

1. N. Hadjiconstantinou, D. Molin, P. Poesio, and G.P. Beretta, Multiscale modeling of spinodal-decomposition-driven mixing, 3rd International Conference "Turbulent Mixing and Beyond", Trieste, Italy, 21-28 August 2011.
2. P. Poesio, D.Molin, N. Hadjiconstantinou, and G.P. Beretta. Macroscale approach to study heat transfer enhancement in small-scale devices, 64th Annual Meeting of APS Division of Fluid Dynamics, Baltimore (Maryland - USA), 20-22 November 2011.
3. P. Poesio, D. Molin, S. Farisè, and G.P. Beretta, Heat transfer in spinodal decomposition: an experimental and numerical work, 50th Meeting of the European Two Phase Flow Group, Udine (Italy), 16-18 May 2012.
4. S. Farisè, A. Franzoni, P. Poesio, and G.P. Beretta, Heat transfer enhancement by spinodal decomposition in micro heat exchangers, Experimental Thermal and Fluid Science, Vol. 42, 38 (2012).
5. S. Farisè, P. Poesio, and G.P. Beretta, Heat Transfer Enhancement by Spinodal Decomposition in Micro Heat Exchangers, Journées d'Etudes des Equilibres entre Phases, JEEP Conference, Nancy (Lorraine, France), 19-21 March 2013.
6. S. Farisè, P. Poesio, and G.P. Beretta, Heat transfer enhancement by liquid-liquid spinodal decomposition in micro heat exchangers, International Conference on Multiphase Flow, ICMF2013, Jeju, Korea, 26-31 May, 2013.
7. G.P. Beretta, Steepest-entropy-ascent and maximal-entropy-production dynamical models of irreversible relaxation to stable equilibrium from any non-equilibrium state. Unified treatment for six non-equilibrium frameworks, 12th Joint European Thermodynamics Conference, Brescia, 1-5 July, 2013, ISBN9788889252222, pp. 100-109.

References

- [Tuckerman and Pease (1981)] D.B. Tuckerman and R.F.W. Pease, High-performance heat sinking for VLSI, IEEE Electron Device Lett. EDL-2, 5, (1981), 126-129.

- [Upadhye and Kandlikar (2004)] H.R. Upadhye and S.G. Kandlikar, Optimization of microchannel geometry for direct chip cooling using single phase heat transfer, Proceedings of the Second International Conference on Microchannels and Minichannels (ICMM2004), 679, (2004).
- [Shah and London (1978)] R.K. Shah and A.L. London, Laminar Flow Forced Convection in Ducts: A Source Book for Compact Heat Exchanger Analytical Data, Academic Press, New York, (1978).
- [Mauri *et al.* (1996)] R. Shinnar, R. Mauri, and G. Triantafyllou. Phys. Rev. E, 53, (1996), 2613.
- [Siggia (1979)] E.D. Siggia, Phys. Rev. A, 20, (1979), 595.
- [Ginzburg and Landau (1979)] V. L. Ginzburg and L.D. Landau, J. Exptl. Theoret. Phys., 20, (1950), 1064.
- [Rowlinson and Waals (1893)] J.S. Rowlinson Waals, Van Der, J. Stat. Phys., 20, (1979), 200.
- [Korteweg (1893)] D.J. Korteweg, Arch. N'eri. Sci. Exactes Nat. Ser., 6, (1901).
- [Cahn and Hilliard (1958)] J.W. Cahn, J. Chem. Phys., 28, (1950), 258.
- [Kawasaki (1958)] K. Kawasaki., Ann. Phys., 61, (1970), 1.
- [Hohenberg and Halperin (1977)] P.C. Hohenberg and B.I. Halperin, Rev. Mod. Phys., 49, (1977), 435.
- [Antanovskii (1996)] L. K. Antanovskii, Physical review E, 54, (1998), 6285.
- [D. M. Anderson *et al.* (1998)] D. M. Anderson, G. B. McFadden, and a. a. Wheeler, Annual Review of Fluid Mechanics, 30, (1996), 139.
- [Emmerich (2008)] H. Emmerich, Adv. Phys., 57, (2008), 1.
- [Kendon *et al.* (1999)] V. Kendon, J-C. Desplat, P. Bladon, and M. Cates. Physical Review Letters, 83, (1999), 576.
- [Kendon *et al.* (2000)] V. Kendon, M. E. Cates, I. Pagonabarraga, J-C. Desplat, and P. Bladon. ArXiv, (2000).
- [Sain and Grant (2005)] A. Sain and M. Grant. Physical Review Letters, 95, (2005), 1.
- [Rosales and Meneveau (2006)] C. Rosales and C. Meneveau. Physics of Fluids, 18, (2006), 075104.
- [Mudawar and Bowers (1999)] I. Mudawar and M.B. Bowers, Ultra-high critical heat flux (CHF) for subcooled water flow boiling-I: CHF data and parametric effects for small diameter tubes, Int. J. Heat Mass Transfer 42, (1999), 1405-1428.
- [Mudawar (2001)] I. Mudawar, Assessment of high-heat-flux thermal management schemes, IEEE Trans. Compon. Pack. Schemes 24, (2001), 122-141.

- [Kandlikar (2005)] S. Kandlikar, High heat flux removal with microchannels: a roadmap of challenges and opportunities, *Heat Transfer Eng.* 26, (2005), 59-68.
- [Kandlikar (2002)] S.G. Kandlikar, Fundamental issues related to flow boiling in minichannels and microchannels, *Exp. Thermal Fluid Sci.*, 26, (2002), 389-407.
- [Wang *et al.* (2004)] E.N. Wang, L. Zhang, L. Jiang, J. Koo, J.G. Maveety, E.A. Sanchez and K.E. Goodson, Micromachined Jets for Liquid Impingement Cooling of VLSI Chips, *Journal of Microelectromechanical System*, 13, (2004), 833-842.
- [Betz and Attinger (2010)] A.R. Betz and D. Attinger, Can segmented flow enhance heat transfer in microchannel heat sinks?, *International Journal of Heat and Mass Transfer* 53, (2010), 3683-3691.
- [Farisé *et al.* (2012)] S. Farisé, A. Franzoni, P. Poesio, and G.P. Beretta, Heat transfer enhancement by spinodal decomposition in micro heat exchangers, *Exp. Thermal and Fluid Science* 42, (2012), 38-45.
- [Duangthongsuk and Wongwises (2009)] W. Duangthongsuk, and S. Wongwises, Heat transfer enhancement and pressure drop characteristics of TiO₂-water nanofluid in a double-tube counter flow heat exchanger, *Int. J. Heat Mass Transfer* 52, (2009), 2059-2067.
- [Pantzali *et al.* (2009)] M.N. Pantzali, A.G. Kanaris, K.D. Antoniadis, A.A. Mouza, S.V. Paras, Effect of nanofluids on the performance of a miniature plate heat exchanger with modulated surface, *Int. J. Heat and Fluid Flow* 30, (2009), 691-699.
- [Brutin and Tadrist (2004)] D. Brutin, and L. Tadrist, Pressure drop and heat transfer analysis of flow boiling in a minichannel: influence of the inlet condition on two-phase flow stability, *Int. J. Heat Mass Transfer* 47, (2004), 2365-2377.
- [Poesio *et al.* (2006)] P. Poesio, G. Cominardi, A.M. Lezzi, R. Mauri, G.P. Beretta, Effects of quenching rate and viscosity on spinodal decomposition, *Phys. Rev. E*, 74, (2006), 011507.
- [Poesio *et al.* (2009)] P. Poesio, G.P. Beretta and T. Thorsen, Dissolution of a Liquid Microdroplet in a Nonideal Liquid-Liquid Mixture Far from Thermodynamic Equilibrium, *Phys. Rev. Letters*, 103, (2009), 06450.
- [Poesio *et al.* (2007)] P. Poesio, A.M. Lezzi and G.P. Beretta, Evidence of heat transfer enhancement induced by spinodal decomposition, *Phys. Rev. E*, 75, (2007), 066306.
- [Gat *et al.* (2009)] S. Gat, N. Brauner and A. Hullman, Heat transfer enhancement via liquid-liquid phase separation, *Int. J. Heat Mass Transfer*, 52, (2009), 1385-1399.
- [Di Fede *et al.* (2011)] F. Di Fede, P. Poesio and G.P. Beretta, Heat transfer enhancement in a mini-channel by liquid-liquid spinodal decomposition, *Int. J. Heat Mass Transfer*, (2011)

- [Molin and Mauri (2007)] D. Molin and R. Mauri, Enhanced heat transport during phase separation of liquid binary mixtures, *Phys. Fluids*, 19, (2007), 074102.
- [Machado and Rasmussen (1987)] E. Machado and P. Rasmussen, Liquid-liquid equilibrium data collection, *DeChema Data Ser. V* (part 4, 52), (1987).
- [Gnielinski (1976)] V. Gnielinski, New equations for Heat and Mass-transfer in turbulent pipe and channel flow, *Int. Chem. Eng.*, 16, (1976), 359-368.
- [Bahramiet *al.* (2006)] M. Bahrami, M. M. Yovanovich, J. R. Culham, Pressure Drop of Laminar, Fully Developed Flow in Microchannels of Arbitrary Section, *ASME J. Fluids Eng.*, 128, September, (2006).
- [Bahramiet *al.* (2007)] M. Bahrami, M. M. Yovanovich, J. R. Culham, A Novel Solution for Pressure Drop in Singly Connected Microchannels, *Int. J. Heat Mass Transfer*, 50, (2007).
- [Akbari and Sinton (2009)] M. Akbari, D. Sinton, M. Bahrami, Pressure Drop in Rectangular Microchannels as Compared With Theory Based on Arbitrary Cross Section, *J. Fluid Eng.*, 131, April, (2009).